Application of Defocusing Technique to Bubble Depth Measurement

Yuki Mugikura

Thesis submitted to the faculty of the
Virginia Polytechnic Institute and State University
in partial fulfillment of the requirements for the degree of

Master of Science

In

Nuclear Engineering

Yang Liu, Chair

Mark A. Pierson

Heng Xiao

May 8, 2016

Blacksburg, VA

Keywords: bubble, depth of field, defocusing

Application of Defocusing Technique to Bubble Depth Measurement

Yuki Mugikura

ABSTRACT

The thesis presents a defocusing technique to extract bubble depth information. Typically, when a bubble is out of focus in an image, the bubble is ignored by applying a filter or thresholding. However, it is known that a bubble image becomes blurred as the bubble moves away from the focal plane. Then, this technique is applied to determine the bubble distance along the optical path based on the blurriness or intensity gradient information of the bubble. Using the image processing algorithm, images captured in three different experiments are analyzed to develop a correlation between the bubble distance and its intensity gradient. The suggested models to predict the bubble depth are also developed based on the measurement data and evaluated with the measured data. When the intensity gradient of the bubble is lower or when a bubble is located farther from the focal plane, the model can predict the distance more accurately. However, the models show larger absolute and relative error when the bubble is near the focal plane. To improve the prediction in that region, another model should be considered. Also, depth of field analysis is introduced in order to compare three experimental results with different imaging setups. The applicability of the approach is analyzed and evaluated.

Application of Defocusing Technique to Bubble Depth Measurement

Yuki Mugikura

GENERAL AUDIENCE ABSTRACT

Gas and liquid measurements of two-phase flow are very challenging, but it has become more important because of many industrial applications such as chemical, petroleum, and energy industries. Many two-phase flow measurement techniques have been developed and utilized for different flow conditions such as fiber optic probe, multi-sensor conductivity probe, wire-mesh sensor, as x-ray densitometry, particle image velocimetry (PIV), and optical imaging. With the development of the technology, the imaging technique can provide better spatial and temporal resolutions as well as image processing speed has improved greatly. In this study, the imaging and defocusing techniques are combined and used to extract bubble depth information. An image processing algorithm has been developed to process bubble images captured by high speed cameras. By measuring the blurriness or intensity gradient information of the bubble, the bubble distance along the optical path is determined. Based on the measurement data, mathematic models are developed to predict the bubble depth. In addition, depth of field analysis is suggested to compare three experimental results with different imaging setups. The applicability of the approach is analyzed and evaluated.

Dedication

To my parents,

Akira and Hideko Mugikura

Acknowledgments

I would like to thank my advisor Dr. Yang Liu for his continuous guidance towards my degree. I truly appreciate the opportunity to work under him to become a better researcher. Also, I must thank my committee members Dr. Mark Pierson and Dr. Heng Xiao for their critical comments and inputs on my research and thesis.

I am also thankful for the members of the Multiphase Flow and Thermal-hydraulics Laboratory (MFTL). Without their help, advice, and some fun, I could not conduct and complete the experiment for my research. Special thanks to Yucheng Fu, Dewei Wang, Kyle Song, Robert Langhans, and Zequn Wang.

I would like to thank my English teacher Hiroshi Masuda in Japan. If I had not met him, I would not even be here today.

Lastly, I would like to thank my parents and my older brothers Hiroto and Hideaki Mugikura for their continuous support and encouragement.

Contents

List of Figures

List of Tables

Chapter 1

1. Introduction

1.1. Background

Gas and liquid measurements of two-phase flow are very challenging, yet it has become more important because such flow occurs in nature and in many industrial applications such as chemical, biochemical, petroleum, energy industries such as power plants and so on. Also, the two-phase flow measurements can be helpful to understand various phenomena. Moreover, such measurement data are used to improve or validate the computational fluid dynamics codes.

At the same time, many two-phase flow measurement techniques have been developed and used for different flow conditions. For example, fiber optic probe [1, 2], multi-sensor conductivity probe [3, 4], wire-mesh sensor [5] are classified as intrusive techniques and are used to measure the particle velocity profile in the bubbly flow. Also, other techniques are non-intrusive such as x-ray densitometry [6, 7], particle image velocimetry (PIV) [8, 9], and optical imaging [10-12]. Since those non-intrusive techniques do not require placing the measuring device into the flow, they can reduce or eliminate the disturbance in the flow field as opposed to intrusive methods. Recently, as the technology has advanced, the capability of the imaging system in terms of the spatial and temporal resolutions as well as image processing speed have improved greatly. However, in many cases, the imaging technique tends to capture only 2-dimensional information. In other words, they process only objects that are in focus and ignore objects if they are out of focus by applying filters or thresholding on the image [12-16].

In contrast, in the field of computer vison, many techniques have been developed to recover the depth information. In this thesis, one of the techniques called defocusing is introduced to the

imaging technique in two-phase measurement [17]. For instance, when an object is placed at the focal plane of the imaging system, the object is in focus and one sees a very clear image of the object as well as the sharp edge of the object. As the object moves away from the focal plane, the image becomes out of focus, blurred, and the intensity of the image decreases. The edge of the object has also blurred and becomes harder to distinguish from the background. But, by setting the focal plane of the imaging system at a specific location and observing how the intensity of the objects change or measuring the blurriness of the object as it moves away from the focal plane, the depth information can be extracted using the defocusing technique.

1.2. Depth Recovery Techniques

One of the most common techniques used in computer vision or robotics for depth perception is stereo imaging [18-21]. The stereo imaging typically utilizes two cameras placed on a common baseline or on a known geometry usually in parallel. Then synchronized cameras capture a pair of images of the same scene from a different angles. By measuring the disparity between two images and the known geometry, the stereo imaging recovers the depth. It often suffers from correspondence problem which can result in an increase of the computational cost. Another type of stereo imaging uses only one camera for 3-dimensional reconstruction [22]. It is done by rotating the camera around a center point of the rotation. The problem with this is that the images cannot be captured at the same time since the camera have to move to record images from the different angles. Moreover, the object in the image needs to be stationary. Another method to recover the depth with a single camera is depth from focus (DFF) [23-26]. The technique requires taking multiple images by changing the focal length, f, or distance between imaging sensor to lens, s_i, or the distance from the object to the lens d_o until the object is in focus.

Once the object is in focus, the depth of the object can be calculated using the thin lens formula with a known geometry.

$$\frac{1}{d_o}+\frac{1}{s_i}=\frac{1}{f}$$

The defocusing technique is applied to the particle tracking anemometry (PTA) in order to examine the 3-dimensional velocity vector [27, 28]. With a wide laser light sheet and setting the focal plane to be front of the sheet, the particles are intentionally defocused when they pass the laser sheet. Then, the size of the defocused images is used to determine the 3-D velocity component.

1.3. Objectives

The main objectives of this thesis are following:

- To develop the image processing algorithm to obtain bubble information by applying the defocusing technique.
- To develop models to correlate the change in intensity and depth information.

1.4. Outline

This thesis is organized as follows:

- Chapter 2 presents a preliminary experiment with a solid acrylic ball, an image processing algorithm, and its result.
- Chapter 3 presents an experiment with a tube gas injection, and describes the image processing algorithm, and its result.

- Chapter 4 presents an experiment with a single hole gas injection system, and describes the image processing algorithm, and its result.
- Chapter 5 introduces the depth of field analysis to compare three different experimental results.
- Chapter 6 summarizes the important conclusions and discusses the future work

Chapter 2

2. Test with Solid Acrylic Ball

2.1. Experimental Setup

The schematic of the test setup is shown in Figure 2.1. The test apparatus is made of an acrylic block with a 30 mm x 10 mm rectangular cross section. The channel is filled with water from the top opening, where a solid acrylic ball attached to an L-shape tube is installed. Water can be drained by opening the valve located at the bottom of the test channel. Transparent measuring tapes are attached on both sides of the test channel wall diagonally. The tapes are used for image calibration and to obtain image resolution.

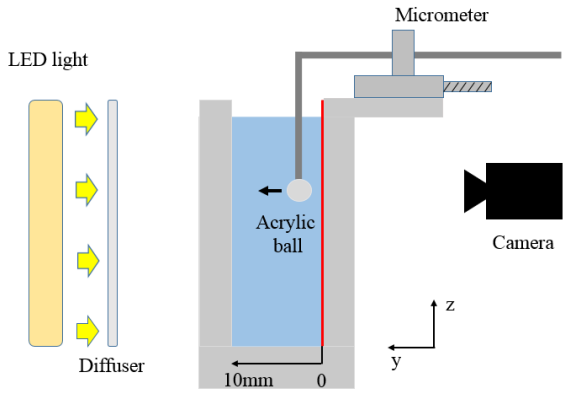

Figure 2.1: Schematic of the test setup.

In this experiment, a solid acrylic ball is used to represent a bubble in the test channel. The acrylic ball is glued to the tip of the L-shape stainless steel tube. The tube is mounted on the tube holder attached to a translational stage as shown in Figure 2.2(a). The position of the tube or the ball is then controlled by a micrometer for precise movements along the optical path of the camera.

Figure 2.2(b) shows the four solid acrylic balls with different diameters used in this experiment. Their diameters are 6.35 mm, 3.975 mm, 3.175 mm, and 1.625 mm.

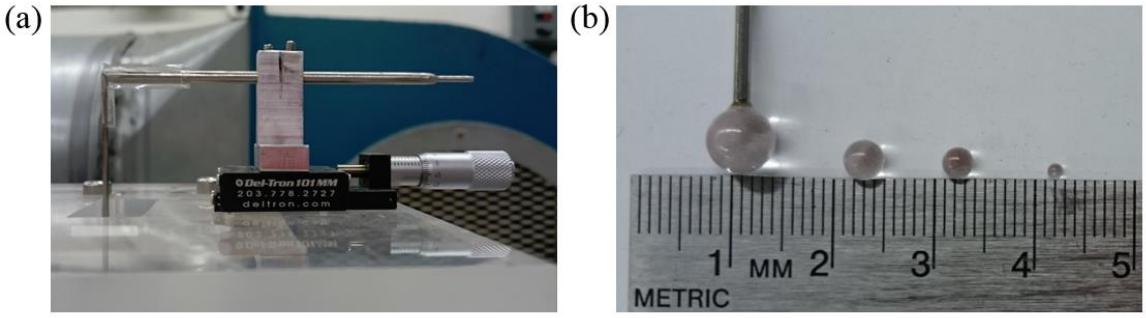

Figure 2.2: (a) L-shape tube mounted on a micrometer and (b) four different size of acrylic balls. The ball on the left is attached to the tip of the tube.

A high speed camera Photron FASTCAM SA4 is used to acquire the acrylic ball images. The SA4 has a CMOS image sensor with a maximum resolution of 1024 x 1024 pixels. The camera is equipped with a TAMRON macro lens with a focal length of 180 mm and placed in front of the test section facing the 30 mm wall. The camera is connected to a PC to acquire images using the Photron FASTCAM Viewer (PFV) software (Photron USA, Inc). A LED light with diffuser is arranged on the opposite side of the camera to provide as uniform of a backlight illumination as possible. The actual images of the test setup are shown in Figure 2.3. The distance between the front wall of the test channel and the camera sensor is measured to be 48.7 cm.

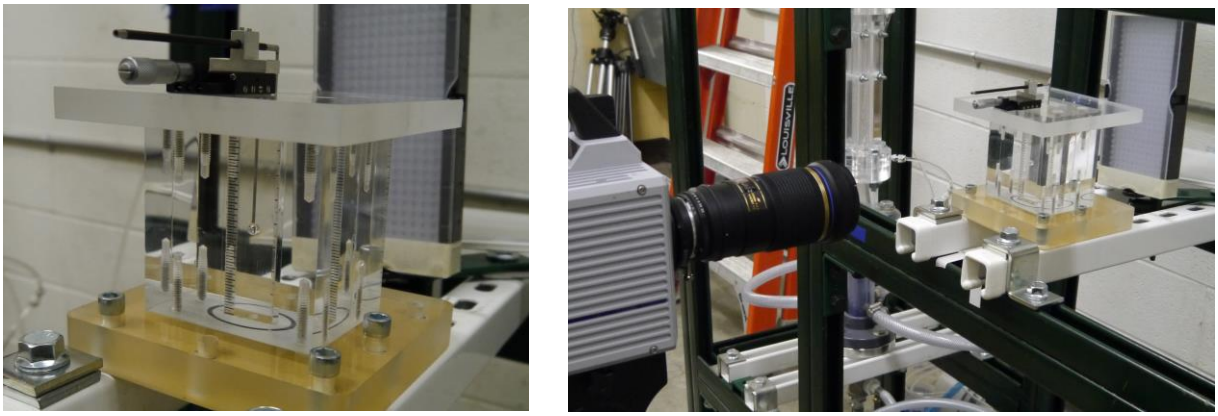

Figure 2.3: Pictures of the test section.

2.2. Test Condition and Procedures

The experiment procedure is described as follows. First, the test channel is filled with water, and a drain valve at the bottom is closed to have no liquid and gas flow in the test section. The focal plane of the image is set to be the front wall. Before inserting each acrylic ball into the test section, background images are recorded, which are used for calibration in later image processing. Then, an acrylic ball is placed inside the test section so that the ball touches the front wall. One image is recorded, and then the ball is moved away from the front wall by 1 mm increments to take additional images. The same steps are repeated until the acrylic ball touches the back wall. Once the acrylic ball reaches the back wall, another acrylic ball is installed to capture images by following the same procedures. Since the ball diameters are different, the number of the locations to capture the images are different too. With 6.35 mm, 3.975 mm, 3.175 mm, and 1.625 mm ball diameters, images are obtained at 5, 7, 8, and 9 locations respectively. The images acquired by the high speed camera are saved as 16-bit Tagged Image File Format (TIFF). Sample images of the acrylic ball with different positions and sizes are shown in Figure 2.4.

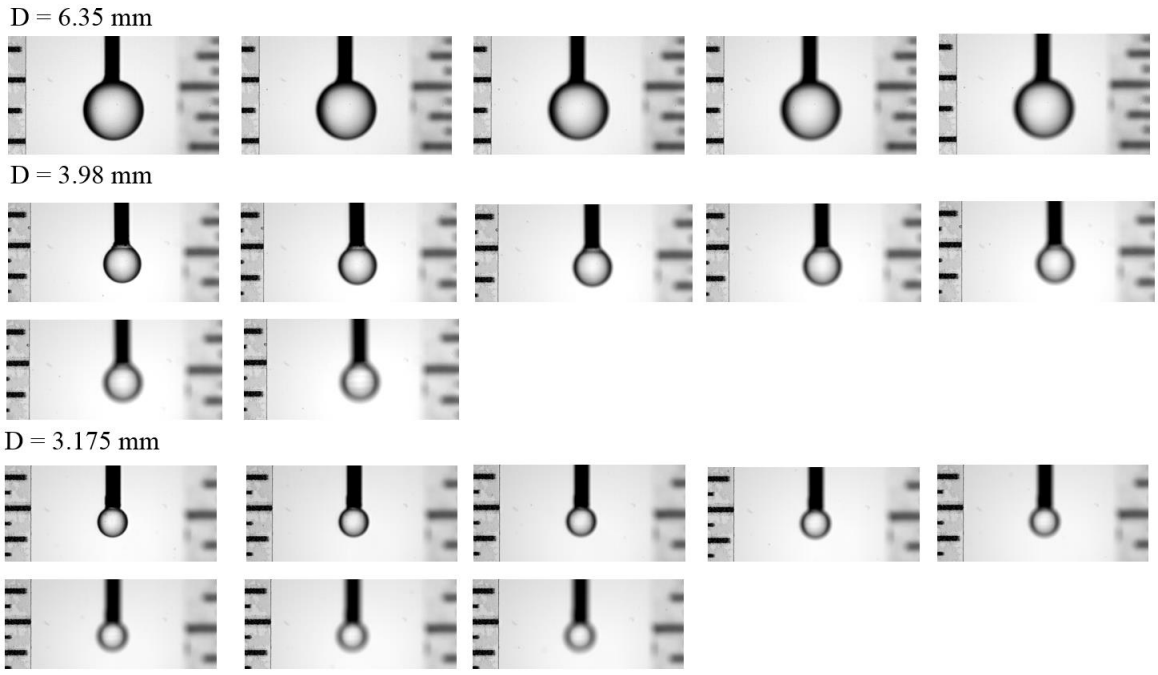

Figure 2.4: Sample bubble images at a different sizes.

2.3. Image Processing

To analyze the recorded images, an image processing algorithm has been developed using MATLAB [29]. Before processing the acrylic ball images, the background images at each ball size, location, and focal plane are processed to obtain average image resolution and maximum intensity gradient at each condition. Figure 2.5(a) shows two sample background images with front and back focus. By comparing the measuring scale which is in focus and the number of pixels which covers the bar of the scale, the average resolution of images with the front and back focal plane is determined to be 46.02 pixels per mm and 45.44 pixels per mm respectively. Figure 2.5(a) shows an intensity gradient map for each sample background image. The red circle is the maximum intensity gradient found on the edge of the measuring tape with magnitude of 3.136 for the front focus and 2.917 for the back focus. The calculation method for the intensity gradient is explained later in this section. The maximum intensity gradient calculated in the background

image is used later to normalize the average gradient around the acrylic ball which is obtained through the image processing algorithm.

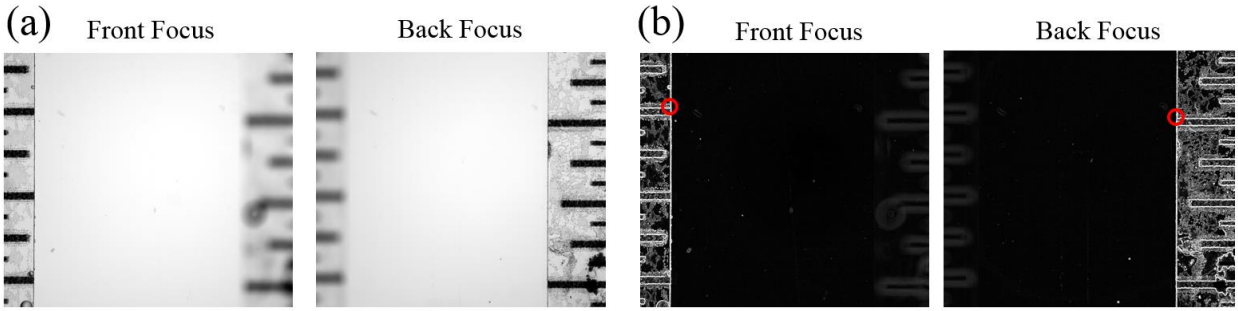

Figure 2.5: (a) Sample background images at front and back focus and (b) intensity gradient map at the front focus. A red circle on the gradient map indicates the maximum gradient found on the scale tape measure.

The main steps for the image processing algorithm are illustrated in Figure 2.6. A sample raw image to describe the steps is shown in Figure 2.6(a). The image is in front wall focus, and its acrylic ball diameter is 6.35 mm. The first step is to normalize the recorded image to reduce non-uniform illumination effects by using the equation:

$$I_N(x,y) = \frac{I(x,y) - I_{Min}}{I_{Max} - I_{Min}} \tag{2.1}$$

where $I_N(x,y)$ and $I(x,y)$ are the normalized intensity value and the original intensity value at the pixel coordinate (x,y). I_{Max} and I_{Min} are the maximum and the minimum intensity value in the entire image respectively. The result is shown in Figure 2.6(b). The normalized image is then cropped into the area of interest to exclude the measuring scale and the top part of the acrylic ball glued to the tube. Figure 2.6(c) shows the cropped image with a resolution of 300 x 400 pixels for this case. The cropped image size depends on the size of ball used. The background noise reduction is achieved by applying a combination of erosion and dilation while minimizing the filtration effect around the bubbles, and its resultant image is shown in Figure 2.6(d).

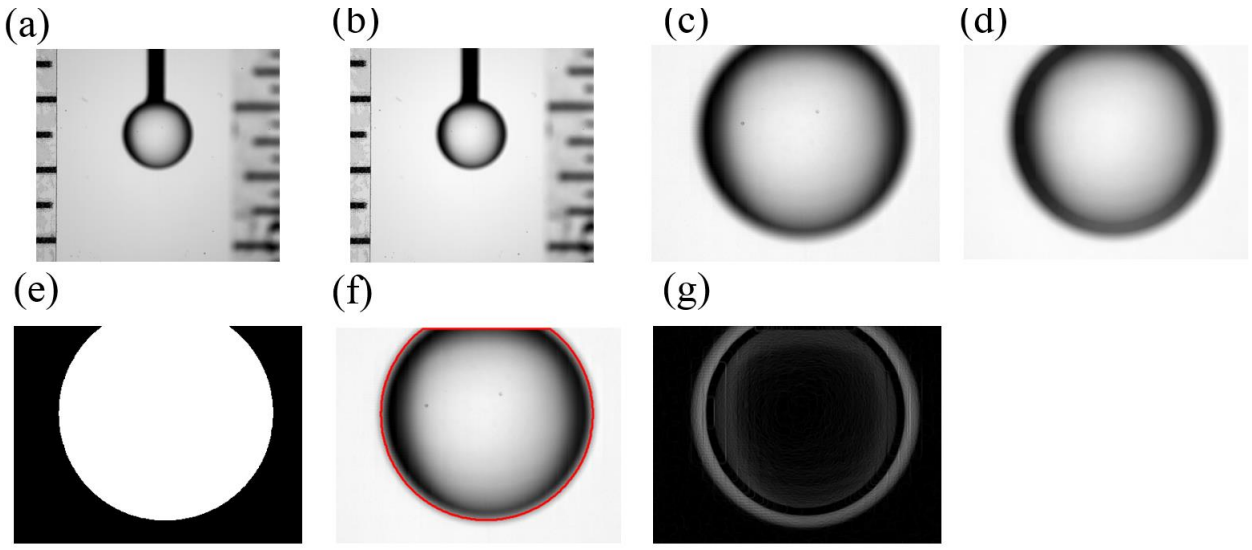

Figure 2.6: (a) Raw image, (b) normalized image, (c) cropped image (d) noise removed image (e) binary image (f) processed images with ball edge on grayscale image, and (g) gradient map

A global threshold is then applied to convert a grayscale image into a binary image using Otsu's method [30]. Figure 2.6(e) shows the binary image after another filtration is applied to remove small objects if any. The white area indicates the acrylic ball detected in the processed image. From the binary images, the ball information such as boundary, area, and the centroid is obtained using the built-in functions in MATLAB. Figure 2.6(f) shows the extracted outline of the acrylic ball on the greyscale image as a red line.

The bubble intensity gradient, G, is calculated using the Sobel gradient operator on normalized grayscale images. The Sobel gradient kernels for the x and y directions are given as:

$$G_x = \begin{bmatrix} -1 & 0 & 1 \\ -2 & 0 & 2 \\ -1 & 0 & 1 \end{bmatrix}, G_y = \begin{bmatrix} 1 & 2 & 1 \\ 0 & 0 & 0 \\ -1 & -2 & -1 \end{bmatrix} \tag{2.2}$$

Then, the magnitude of the intensity gradient is calculated using the convolution kernel as:

$$G = \sqrt{(G_x * I)^2 + (G_y * I)^2} \tag{2.3}$$

where I represents image intensity and "*" is the convolution operator. A sample gradient map is shown in Figure 2.6(g). Instead of using the intensity gradient at the outline coordinates and averaging the values, the algorithm searches for the maximum gradient around each outline coordinate. To do so, an $n \times n$ neighborhood block, where n is an odd number, is defined. Then, the algorithm picks the first element of the outline coordinate to be the center of the neighborhood block and finds the maximum intensity gradient within the block. Once the maximum gradient is determined, the gradient value for that element is replaced by that maximum value. Then, the neighborhood block moves to the next outline coordinate element and does the same operation. Once all the maximum intensity gradients near the outline coordinates are obtained, the average intensity gradient of the acrylic ball is calculated by taking the average of those intensity gradient values. After that, each average intensity gradient is normalized by dividing the value by the maximum intensity gradient calculated in the background image processing parts. Thus, each ball is assigned one intensity gradient value with corresponding distance from the front wall.

Y-distance from the front wall or the object depth information is obtained based on the ball radius and micrometer measurement. If a ball with a diameter of 6.35 mm is placed at the first position touching the front wall of the test channel, the *y*-distance of the ball is recorded as 3.175 mm. With 1 mm increment, the *y*-distance for the next position is recorded as 4.175 mm and so on. The obtained information is analyzed further in the next step.

2.4. Regression Modeling

To estimate the relationship between the depth information, intensity gradient, and the diameter of a solid acrylic ball, two regression models are suggested here.

$$D = C_1 d + C_2 \frac{1}{G} + C_3 \tag{2.4}$$

and

$$D = C_1 d + C_2 \ln(G) + C_3 \tag{2.5}$$

where D is the measured ball distance from the front wall of the test channel, d is the acrylic ball diameter, G is the average intensity gradient calculated from the image processing, C_1, C_2, and C_3 are unknown coefficients that depend on the measurement data. These coefficients for each model are obtained by rewriting Equation (2.4) in the form of a matrix equation:

$$\begin{bmatrix} D_1 \\ \vdots \\ D_N \end{bmatrix} = \begin{bmatrix} d_1 & \frac{1}{G_1} & 1 \\ \vdots & \vdots & \vdots \\ d_N & \frac{1}{G_N} & 1 \end{bmatrix} \begin{bmatrix} C_1 \\ C_2 \\ C_3 \end{bmatrix} \tag{2.6}$$

$$\begin{bmatrix} C_1 \\ C_2 \\ C_3 \end{bmatrix} = \begin{bmatrix} d_1 & \frac{1}{G_1} & 1 \\ \vdots & \vdots & \vdots \\ d_N & \frac{1}{G_N} & 1 \end{bmatrix}^{-1} \begin{bmatrix} D_1 \\ \vdots \\ D_N \end{bmatrix} \tag{2.7}$$

where N is the total number of the data point. By solving Equation (2.7), the coefficients are determined. The coefficients for Equation (2.5) are determined in the same way by solving the following equation:

$$\begin{bmatrix} C_1 \\ C_2 \\ C_3 \end{bmatrix} = \begin{bmatrix} d_1 & \ln(G_1) & 1 \\ \vdots & \vdots & \vdots \\ d_N & \ln(G_N) & 1 \end{bmatrix}^{-1} \begin{bmatrix} D_1 \\ \vdots \\ D_N \end{bmatrix} \tag{2.8}$$

2.5. Results

During the experiment 58 images, 29 images each for the front and back wall focus condition, are recorded and processed. The solid acrylic ball distance to the front wall versus its averaged intensity gradient for each ball diameter is plotted in Figure 2.7. For all cases, the intensity gradient decreases as the ball moves away from the focal plane as expected. When the ball is closer to the focal plane, the change in distance is smaller as the intensity gradient decreases. But, as the acrylic ball moves farther, the magnitude of the slope becomes larger and steeper. In other words, the distance becomes more sensitive to the change in intensity gradient of the image. Also, the size of the acrylic ball has some effect on the result. In the front wall focus case, the larger acrylic ball tends to have a larger normalized intensity gradient at the same distance from the front wall when the ball is located away from the focal plane. But, the size effect becomes less noticeable as the ball size decreases when comparing the result of the ball diameters of 3.175 mm and 1.626 mm. Also, those two data points merge together as the distance is less than 3 mm.

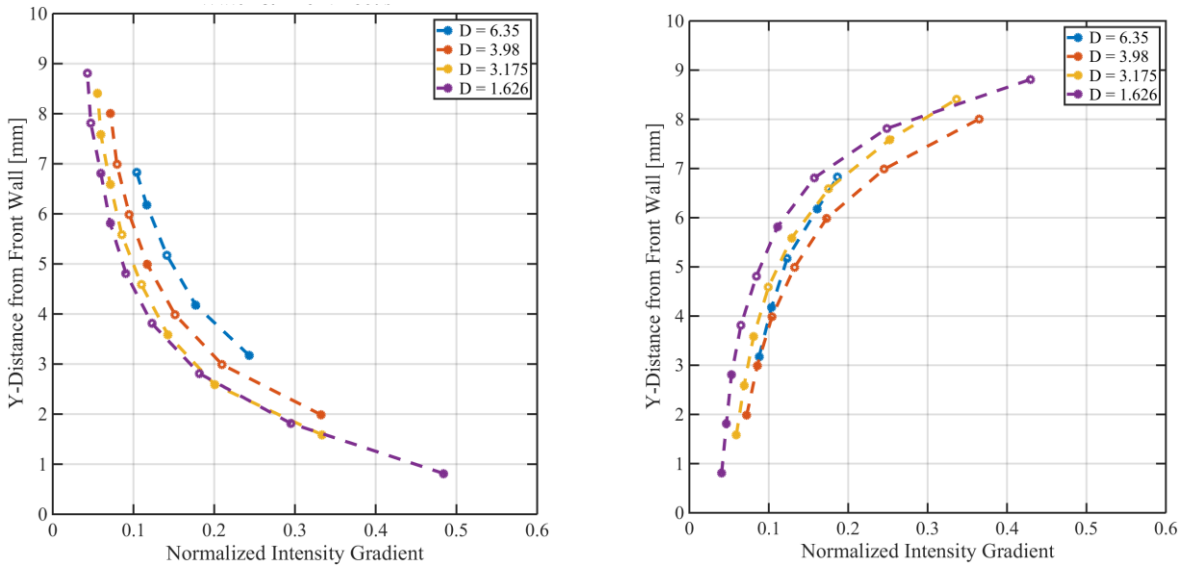

Figure 2.7: Acrylic ball distance versus normalized intensity gradient at (a) front wall focus and (b) back wall focus

The data points are also used to determine the coefficients for the suggested two models. By substituting the distance and intensity gradient data into Equation (2.7) and (2.8), the coefficients for Equation (2.4) and (2.5) are calculated and shown in Table 2.1.

Table 2.1: Coefficients for Equation (2.4) and (2.5)

	C_1	C_2	C_3
Equation (2.4)	0.4845	0.4051	0.6711
Equation (2.5)	0.2931	-3.4750	-3.3669

In Figure 2.8, the predicted distances to the front wall calculated by Equation (2.4) and (2.5) with the coefficients are compared with the measured acrylic ball distances for each ball size. In both cases, measured and predicted distance are within an acceptable range.

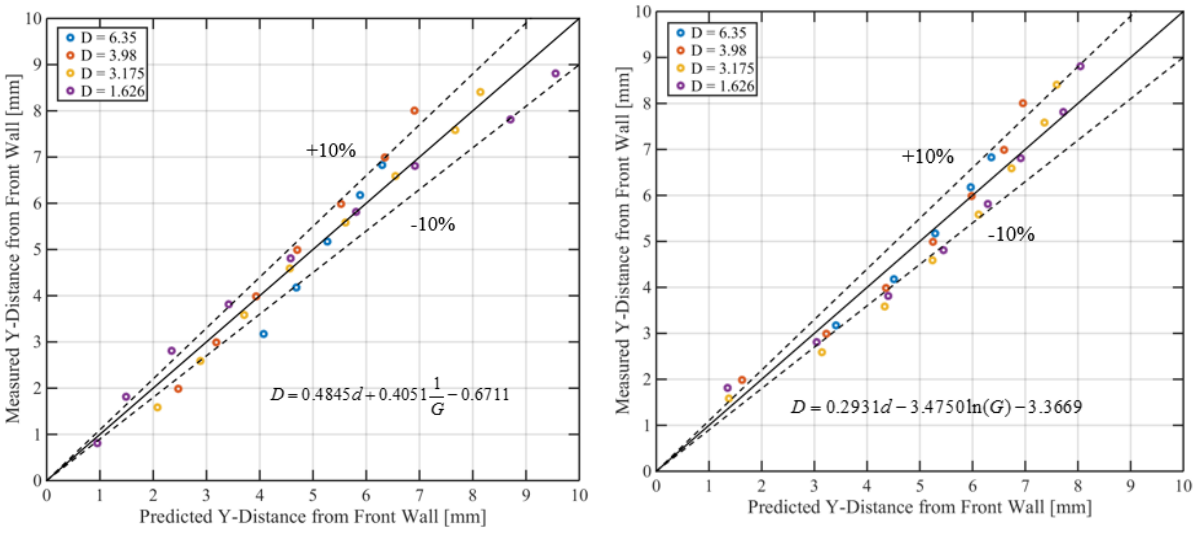

Figure 2.8: Comparison between the measured and predicted normalized intensity gradient using Equation(2.4) and Equation(2.5).

Chapter 3

3. Test with Tube Gas Injection

3.1. Experimental Setup

The schematic of the experimental facility for this test is shown in Figure 3.1. The test section is made of acrylic blocks and designed to operate for air-water two-phase flow in up-flow at atmospheric pressure and room temperature. The height of the test channel is 3.0 m tall and has 30 mm x 10 mm rectangular cross section. There are three visualization ports and instrumentation ports at z/D_h = 8.8, 72.4 and 136 with the hydraulic diameter of the test channel D_h = 15 mm. A water pump and valves are used to change and adjust the flow rate. There are two magnetic flow meters to measure the water flow rate into the test channel with an accuracy of ±1%. Air flow is supplied by the building through the compressed air line and controlled by a pressure regulator. The air flow rate is measured by an air flow meter with an accuracy of ±1% of the reading. Different bubbly flows can be obtained by controlling the water and air flow rates in the test loop.

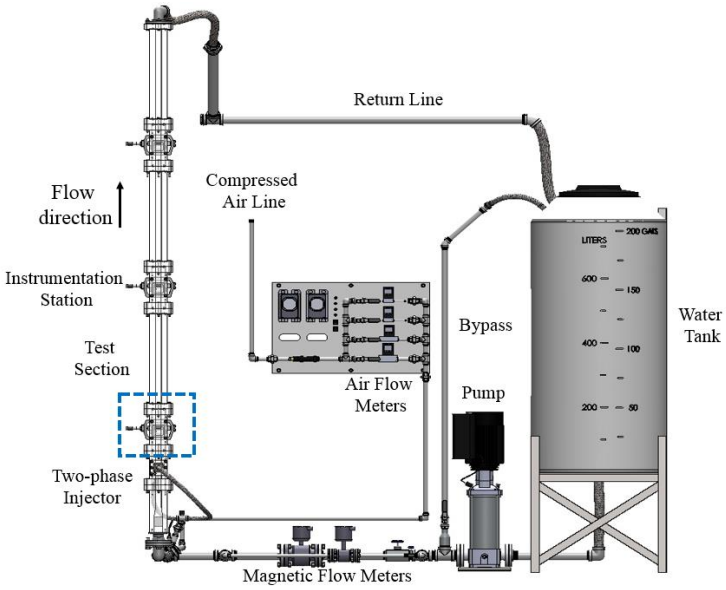

Figure 3.1: Schematic of the rectangular test loop.

To generate bubbles, a stainless steel tube which has a 90° elbow is used. The tube has an inner diameter of 1.37 mm and an outer diameter of 1.83 mm. One side of the tube is connected to the air line, and its elbow side is inserted into the middle of the 30 mm wall side of the test section as shown in Figure 3.2(a). The tube is mounted on the micrometer stage to position the tube accurately across the test section. Figure 3.2(b) shows the top view of the imaging system. The focal plane for the front camera is set at the front wall of the test section. For the side camera, the focal plane is set to the middle of the test section where the bubbles are generated.

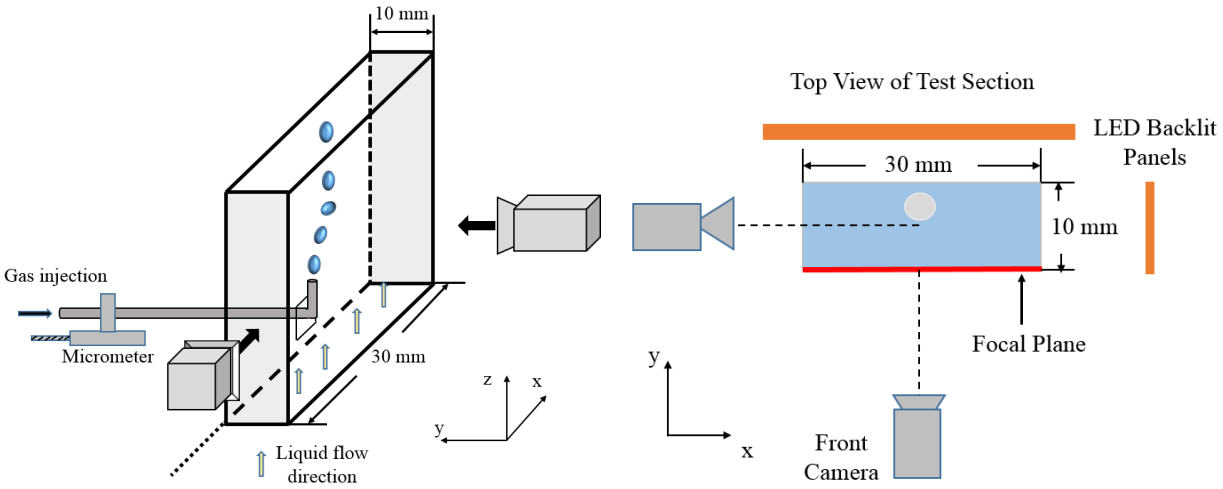

Figure 3.2: (a) Gas injection design, (b) top view of the imaging system

In this test, two high speed cameras (Photron FASTCAM SA6 and SA4) are used to record bubbles generated at the first port (z/D_h = 8.8). The SA6 with a resolution of 1920 x 1440 pixels is placed in front of the test section facing the 30 mm wall. The SA4 with a resolution of 1024 x 1024 is placed on the side facing the 10 mm wall. The SA6 has a 105 mm Nikon lens, and the SA4 has a 55 mm Nikon Micro-NIKKOR lens. The two cameras are connected and synchronized to capture images at the same time via PFV software. Figure 3.3(a) is a calibration image from the front camera showing the measuring tape attached to the front wall or the focal plane of the camera. By comparing the reading on the scale bar and the number of pixels which covers the bar,

the average resolution of images is determined to be 102.7 pixel per mm. Similarly, the average image resolution for the side image is determined based on the width of the test channel and the number of pixels covering the distance. As shown in Figure 3.3(b), it takes 287 pixels to cover 10 mm width of test section in the side image. Thus, the average resolution of the side image is 28.7 pixel per mm. Two LED lights are placed on the opposite side of the each camera to provide the backlight illumination. The distance from the focal plane to the front camera imaging sensor is measured to be 52.2 cm in this experiment.

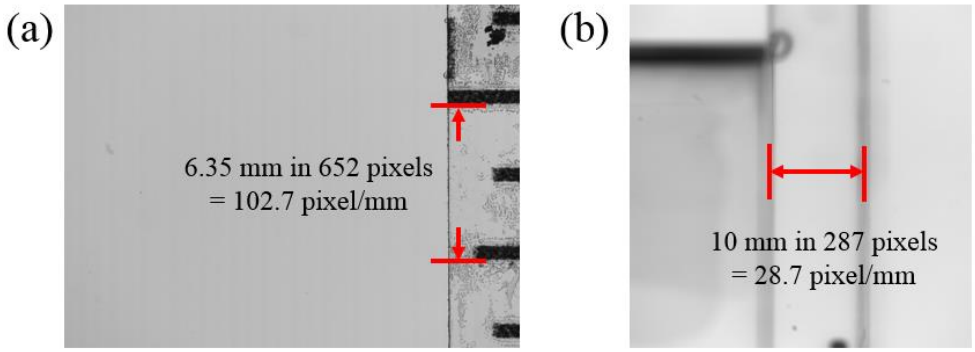

Figure 3.3: Calibration image (a) from the front camera with measuring scale and (b) from the side camera with known width of 10 mm

3.2. Test Condition and Procedures

Bubble images are recorded in stagnant water flow with fixed gas flow rate in this experiment. The gas flow rate is fixed at 89.6±0.2 cm^3/min. Before running the test loop, the gas injection tube is installed and placed in the test channel where the tube touches the wall facing near the front camera. After recording bubble images at that location, the tube is moved backward from the wall to another location with 1.0 mm increments. In total, seven test runs at different gas injection locations are performed in this experiment.

The two high speed cameras are synchronized to capture the bubbles at the frame rate of 1000 frames per second, and 100 images are aquired at each tube location. All the images are

saved as 16-bit TIFF. Sample images recorded by the front and the side camera at different gas injection locations are shown in Figure 3.4. The front images are processed to obtain the intensity gradient information of the bubbles, and the side camera images are used to extract depth information of the bubbles. From the background image capture by the front camera, the magnitude of the maximum intensity gradient is calculated to be 2.236 and the value is used to normalize the intensity gradient of bubbles in the image processing.

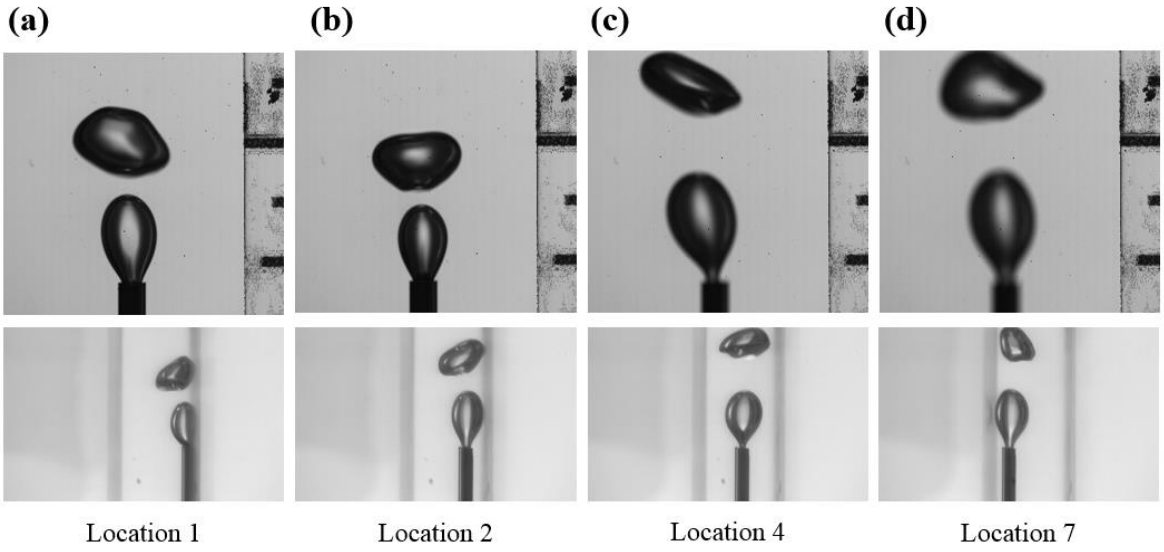

Figure 3.4: Sample bubble image at different distance from the focak okane recorded by the front and side camera.

3.3. Image Processing

The basic image processing procedures are similar to the one explained in Chapter 2. The main difference is to process images obtained by the side camera to extract the depth information. Also, in case multiple bubbles appear in an image, it is necessary to identify bubbles in the front and side images and determine the corresponding bubble in each image. Figure 3.5 shows a simple image processing flow chart.

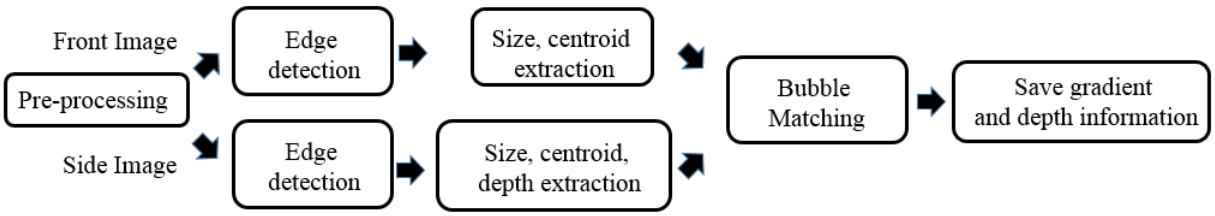

Figure 3.5: Image processing flow chart

In the pre-processing, the recorded raw images are normalized using Equation (2.1) to minimize non-uniform illumination effects shown in Figure 3.6(a) and (b). Both front and side images are cropped into regions of interest. Then, small background noises are removed by using the erosion and dilation function in MATLAB. The resultant images are shown in Figure 3.6(c). The front image has a size of 1010 x 1320 pixels. By dividing it by the image resolution of 102.7 pixel per mm, the imaging size in mm scale is expressed as 9.83 x 12.85 mm. Similarly, the side images are cropped into the size of 287 x 368 pixels which are equal to 10 x 12.82 mm.

By applying a global threshold, a cropped grayscale image is converted into a binary image as shown in Figure 3.6(d). For the front image, the bubble intensity gradient is obtained by using Equation (2.2) and (2.3), and the gradient map is shown in Figure 3.6(e). At this step, a growing bubble attached to the gas injection tube is also identified as seen in the sample image, but only bubbles detached from the tube are analyzed to simplify the processing. From the side image, bubble information such as outline, centroid, and size of detected bubbles are determined. When multiple bubbles are detected, the vertical coordinate of the bubble centroid is compared to find the same bubble in the front and the side images. Figure 3.6(f) shows the extracted outline of the bubble on the front and side greyscale image in a red line. The centroid of the bubble in the side image is marked as a blue dot.

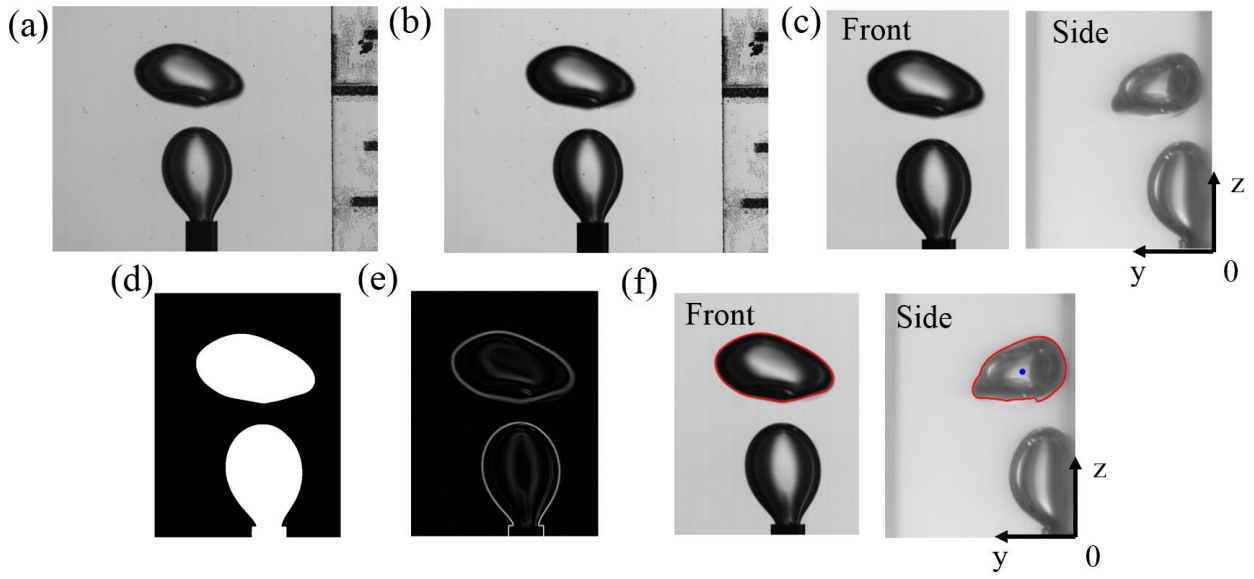

Figure 3.6: (a) Raw image, (b) normalized image, (c) cropped and noise removed image, (d) binary image, (e) intensity gradient map, and (f) processed front and side images with bubble edge. In the side image, the centroid of bubble is shown as "*".

Once matching bubbles in the two images are identified, the bubble intensity gradient is calculated using the same method as explained in Chapter 2. At each outline coordinate, the algorithm searches the maximum intensity gradient in a 9×9 neighborhood block having the outline coordinate as a center pixel. The maximum gradient value is assigned to the outline coordinate. Then, the block slides to the next outline coordinate and does the same operation. The processed data of the bubbles, the average intensity gradient and the distance to the front wall, are stored and used to develop a correlation model explained in the next section.

3.4. Data Analysis and Results

For this experiment, the correlation between bubble distance *D* and its intensity gradient *G* are modeled using a log function and an exponential function as:

$$D = C_1 + C_2 \ln(G) \tag{3.1}$$

$$D = C_1 e^{C_2 G} \tag{3.2}$$

where C_1, and C_2, are adjustable parameters determined by the imaging condition. To calculate the coefficients, the equation is rewritten in matrix form as:

$$\begin{bmatrix} D_1 \\ \vdots \\ D_N \end{bmatrix} = \begin{bmatrix} 1 & \ln(G_1) \\ \vdots & \vdots \\ 1 & \ln(G_N) \end{bmatrix} \begin{bmatrix} C_1 \\ C_2 \end{bmatrix}$$

$$\begin{bmatrix} C_1 \\ C_2 \end{bmatrix} = \begin{bmatrix} 1 & \ln(G_1) \\ \vdots & \vdots \\ 1 & \ln(G_N) \end{bmatrix}^{-1} \begin{bmatrix} D_1 \\ \vdots \\ D_N \end{bmatrix} \tag{3.3}$$

By solving Equation(3.3), the coefficients C_1 and C_2 are calculated. The coefficients for Equation (3.2) are determined in the same way as follows:

$$\ln(D) = \ln(C_1) + \ln(e^{C_2 G})$$

Let $C_1^{'} = \ln(C_1)$,

$$\ln(D) = C_1^{'} + C_2 G$$

$$\begin{bmatrix} \ln(D_1) \\ \vdots \\ \ln(D_N) \end{bmatrix} = \begin{bmatrix} 1 & G_1 \\ \vdots & \vdots \\ 1 & G_N \end{bmatrix} \begin{bmatrix} C_1^{'} \\ C_2 \end{bmatrix}$$

$$\begin{bmatrix} C_1^{'} \\ C_2 \end{bmatrix} = \begin{bmatrix} 1 & \ln(G_1) \\ \vdots & \vdots \\ 1 & \ln(G_N) \end{bmatrix}^{-1} \begin{bmatrix} \ln(D_1) \\ \vdots \\ \ln(D_N) \end{bmatrix} \tag{3.4}$$

For this experiment, instead of using all the data points to determine those coefficients, the distance and intensity gradient information is processed as follows. From the image processing, a total of 805 bubbles are processed. The bubble distance from the front wall versus its normalized intensity gradient is plotted in Figure 3.7(a). Those data points are divided into small intensity gradient intervals shown in Figure 3.7(b). Then, the averaged gradient and the distance are calculated within 0.01 intensity intervals.

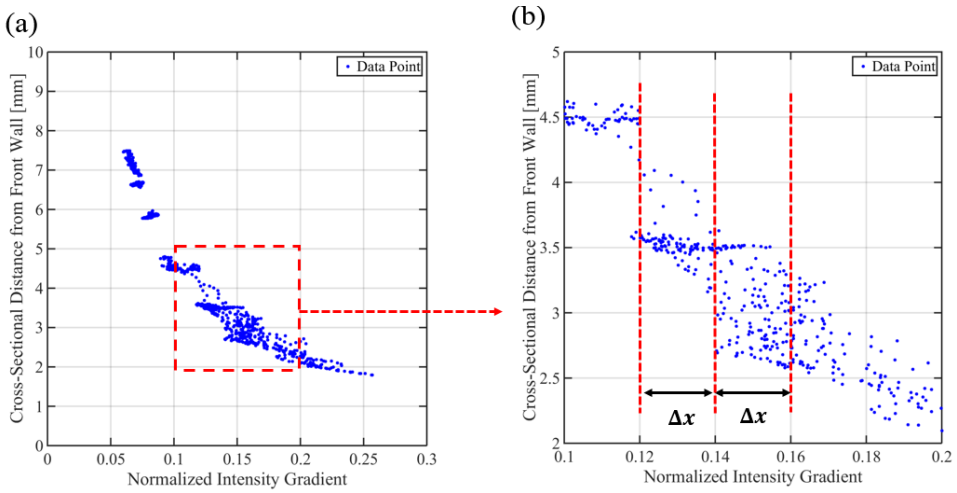

Figure 3.7: (a) Intensify gradient of 805 bubbles (b) divided data points with an interval of Δx=0.01

In the previous experiment, only one equation is used to predict the distance of the acrylic ball within the 10 mm range. But, it is found that, the distance becomes more sensitive to the image intensity gradient change as the acrylic ball moves away from the focal plane. To capture such tendency the data points are divided into two regions less than or greater than 4 mm for this experiment. Equation (3.1) is used to describe the region greater than 4 mm, and Equation (3.2) is for the region less and 4mm. To calculate the coefficients for each region, the averaged distance and its intensity gradient are substituted into Equation (3.3) and (3.4). The calculated coefficients for the two curves are shown in Table 3.1. Also, using Equation (3.1) and (3.2) with the coefficients, two curves are plotted in Figure 3.8 with the averaged data points as green dots.

In the figure, the curve for distance between 4 mm and 10 mm has the steeper slope as observed in the previous test. The curve shows good agreement with the average data points. On the other hands, the curve for less than 4 mm captures the trend that the slope become less steeper, but does not have as good agreement with the averaged data points, especially near the front wall and the intersection of the two curves.

Table 3.1: Calculated coefficients for two curves

	C_1	C_2
Curve 1 [0 mm 4 mm]	2.01040	-5.77020
Curve 2 [4 mm 10 mm]	-7.70697	-5.43983

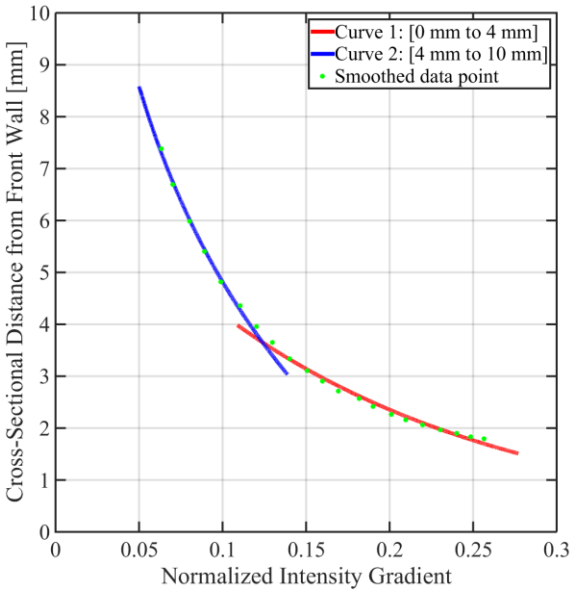

Figure 3.8: Fitted curves for two regions below and above 4 mm with averaged data point

Figure 3.9(a) shows the comparison between the average measured distance to the front wall and the predicted distance using the log model. As mentioned above, the measured distances above 4 mm have good agreement with the predicted curve, but relatively large difference between measured and predicted data points below 4 mm. In Figure 3.9(b), the individual measured distances are also compared with the predicted distance calculated using the predicted curves. As shown in Figure 3.10, the absolute error varies from -0.11 mm to 0.18 mm with the curve for below 4mm. For the curve above 4 mm, it shows smaller absolute error which is between -0.05 mm to 0.08 mm. In terms of the relative error, the mean relative error is 2.23 % with the highest error of about 6 %. Especially, above 4 mm the relative error is smaller than 2 %. These results shows

that the fitted curve for above 4 mm predicts the bubble distance with a reasonable accuracy, but not the fitted curve below 4 mm.

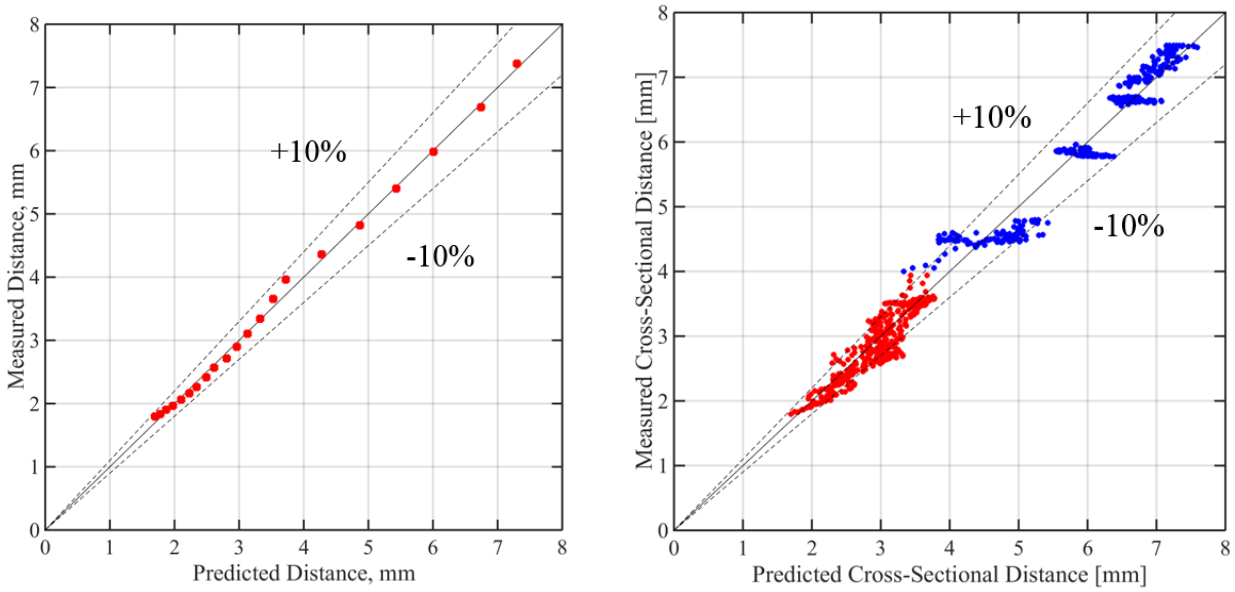

Figure 3.9: Comparison of measured distance versus predicted distance with (a) averaged data point and (b) individual data points

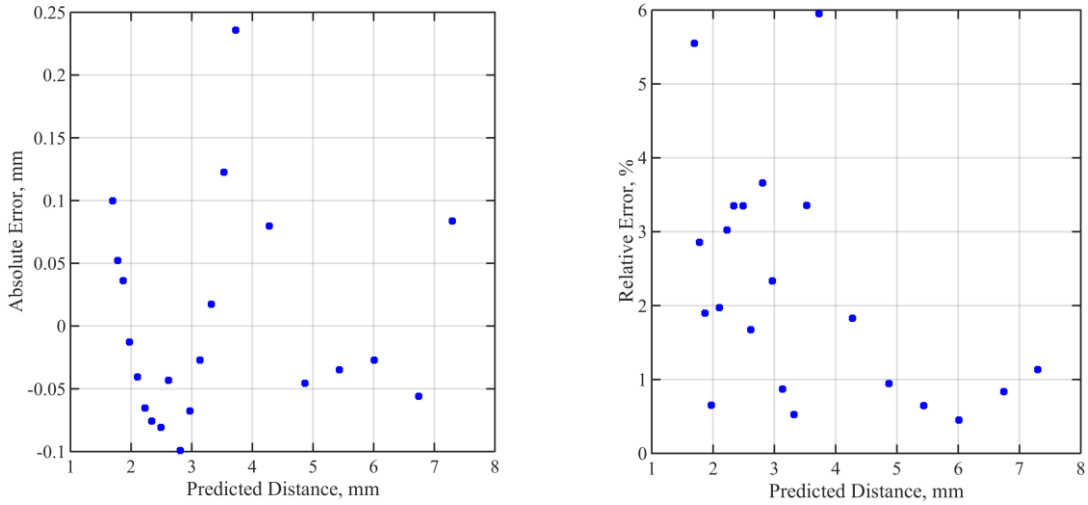

Figure 3.10: (a) Absolute error and (b) relative error

Chapter 4

4. Test with a Single Injection Hole on the Wall

4.1. Experimental Setup

This experiment is conducted with the same test facility as shown in Figure 3.1, but a different bubble generation system is used. Figure 4.1(a) shows the gas injection design for this experiment. Instead of using an L-shaped tube, a thin acrylic plate is installed against the 30 mm at the same location as the tube was installed in the previous experiment. The thin plate has a single 100 μm hole drilled at the center of the plate for gas injection. Figure 4.1(b) shows the top view of the imaging system. The same as the previous test, the focal planes for the front camera are set to the front wall and to the middle of the test section where bubbles are generated.

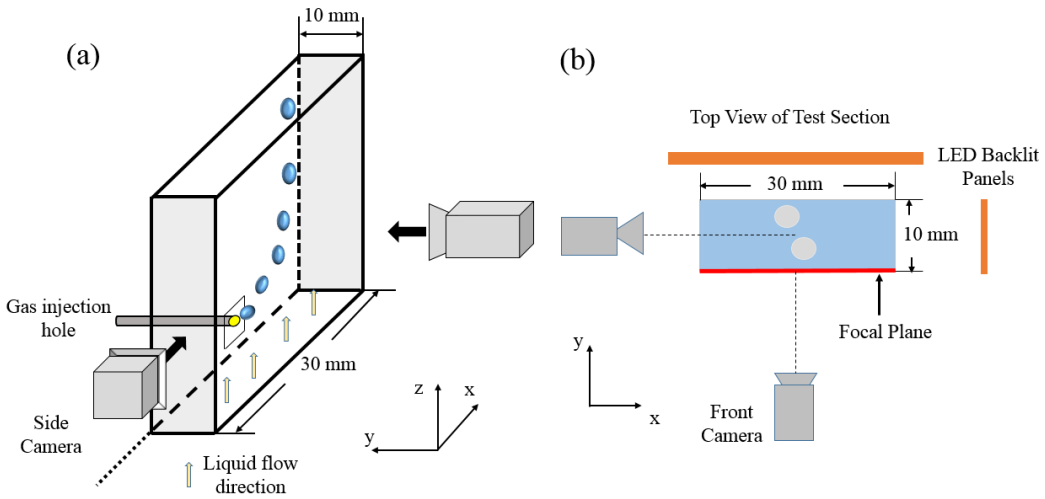

Figure 4.1(a) Gas injection design and high speed cameras' set up (b) top view of the imaging system

In this test, two high speed cameras (Photron FASTCAM SA6 and SA4) are used to record bubbles generated at the first port (z/D_h = 8.8). The same as the previous experiment, the SA6 and

SA4 are placed in front of the test section facing the 30 mm wall and on the side facing the 10 mm wall respectively. Figure 4.2(a) is a calibration image from the front camera with average resolution of the image of 80.75 pixel per mm. Similarly, Figure 4.2(b) shows the resolution of the side image to be 27.3 pixel per mm. Two LED lights are placed on the opposite side of each camera for backlight illumination.

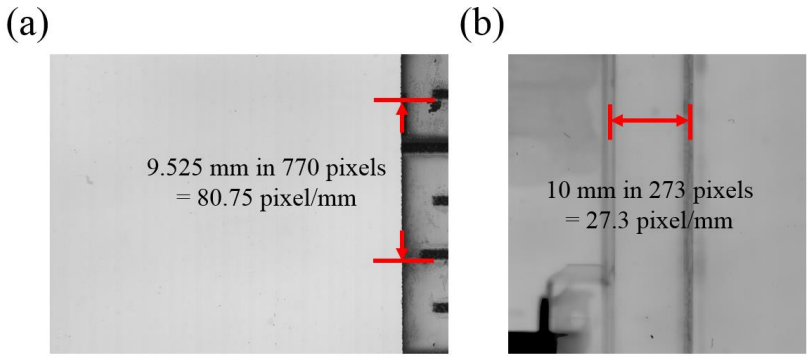

Figure 4.2: Calibration image (a) from the front camera with measuring scale and (b) from the side camera with known width of 10 mm

4.2. Test Condition and Procedures

The experiment was conducted with a fixed gas flow rate of 54.8 cm^3/min and liquid flow rate from 0.0 cm^3/min to 36 cm^3/min given in Table 4.1. For each condition, the two high speed cameras capture the bubbles at the frame rate of 1000 frames per second, and 450 images are acquired. As mentioned earlier, all images from the front and side cameras are saved as 16-bit TIFF. Figure 4.3 shows the images recorded by the front and the side camera at different flow conditions. In the same way as the previous test, the front images are processed to extract the intensity gradient information of the bubbles, and the side images are used to extract depth information of the bubbles.

Table 4.1: Gas and liquid flow rate condition

	Water flow rate, cm^3/s	Gas flow rate, cm^3/s
Run 1	0	54.8
Run 2	19	54.8
Run 3	36	54.8

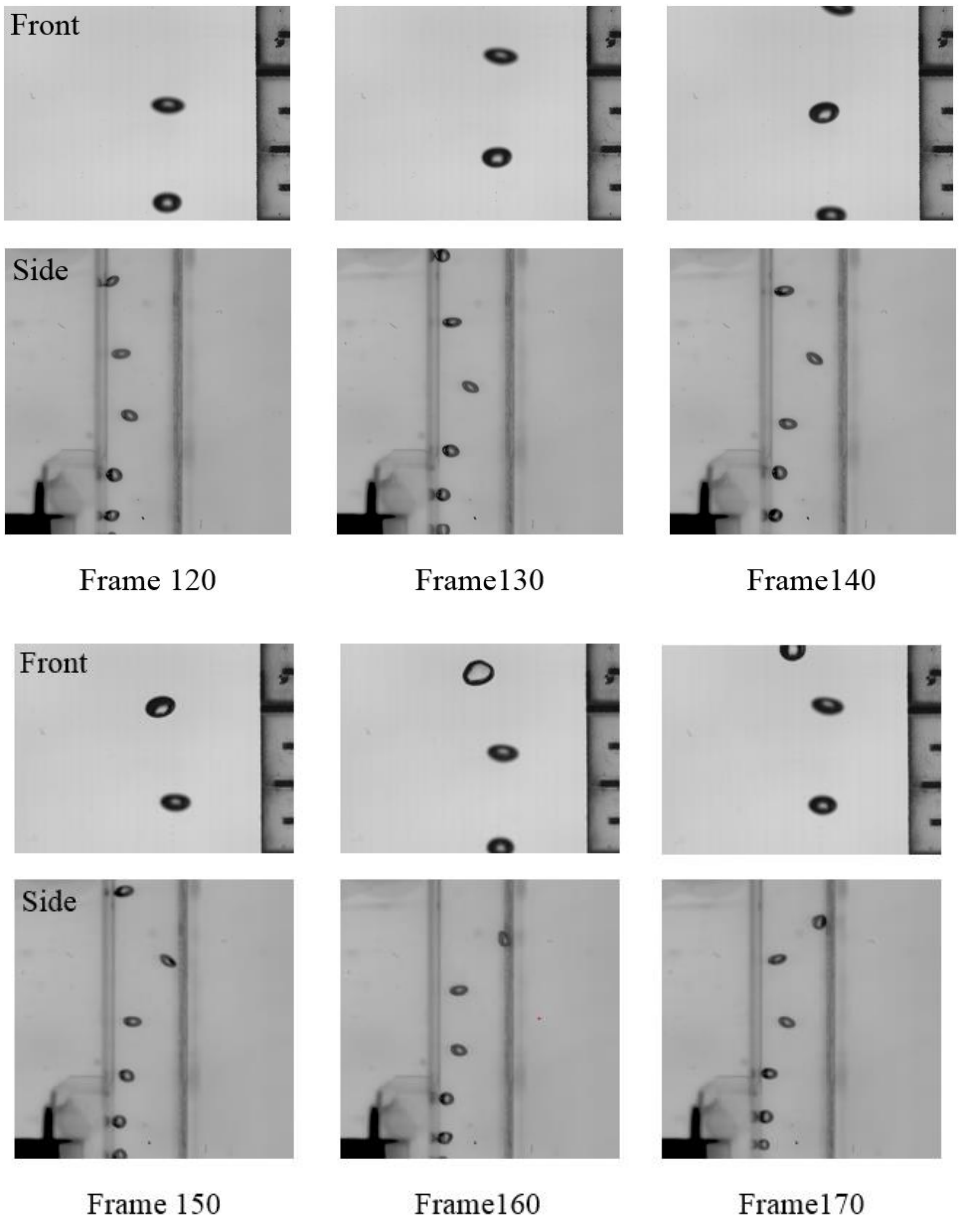

Figure 4.3: Raw sample front and side images for Run 1

Also, the magnitude of the maximum intensity gradient in the background image is calculated to be 1.888 which is used to normalize the intensity gradient of the bubbles in the image processing.

4.3. Image Processing

The image processing procedure is the same as explained in Chapter 3 and follows the flowchart shown in Figure 3.5. An example of image processing is shown in Figure 4.4. First, a raw grayscale image is cropped into the area of interest. The raw image is then normalized using Equation(2.1). Small noise is removed by applying erosion and dilation operations on the normalized image shown in Figure 4.4(c). To detect bubbles, the image is converted into a binary image based on a global thresholding level. Once the bubbles are detected, the edge, area, and the centroid of bubble are extracted from the binary image. The horizontal coordinate of the centroid obtained from the side image is used to determine the distance to the front wall. The Sobel operator is applied to the normalized image to obtain the gradient map. As explained in Chapter 2, the algorithm looks for the maximum intensity gradient near each outline coordinate and replaces the original gradient value by the maximum gradient value in the neighborhood. The same search area as the previous two tests is used, which is a 9×9 matrix. Then, the average intensity gradient around the bubble edge is calculated. To match bubbles in the front and side images, the vertical coordinate of centroid is compared if their coordinates are within the same range. Figure 4.4(f) shows the result of image processing for an image with two bubbles. The outline of the detected bubbles in front and side images are indicated as red lines. Also, the matching bubbles are labeled with the same numbering in both images.

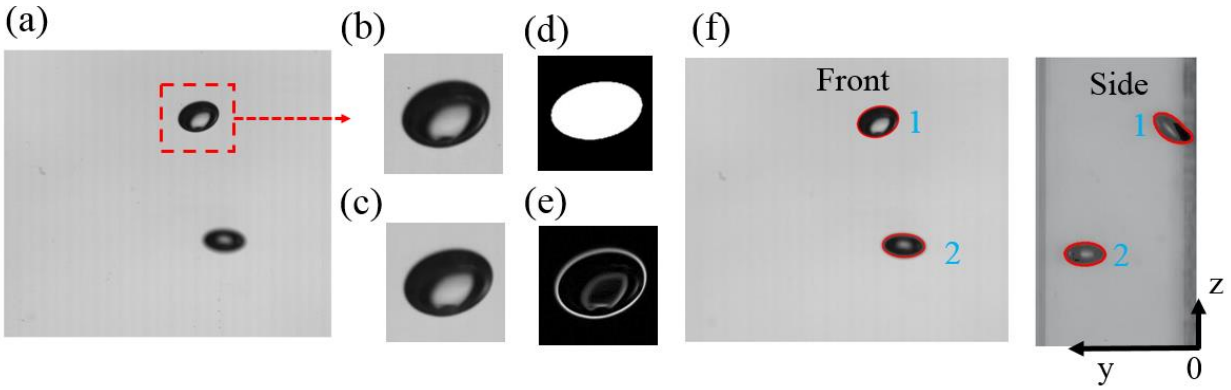

Figure 4.4:(a) Raw image, (b) a raw bubble image, (c) normalized image, (d) binary image, (e) intensity gradient map, (f) processed front and side images with bubble edge and corresponding numbers.

4.4. Results

In order to examine the correlation between the distance to the focal plane and its intensity gradient, a total of 3279 bubbles were processed. Figure 4.5(a) is the plot of the bubble distance to the focal plane versus its averaged intensity gradient. The same as in the experiment with tube gas injection, these data points are divided into a small intensity gradient interval of 0.02 as shown in Figure 4.5(b). Then, the distance and gradient within the intervals are averaged, and the result is plotted in Figure 4.5(c).

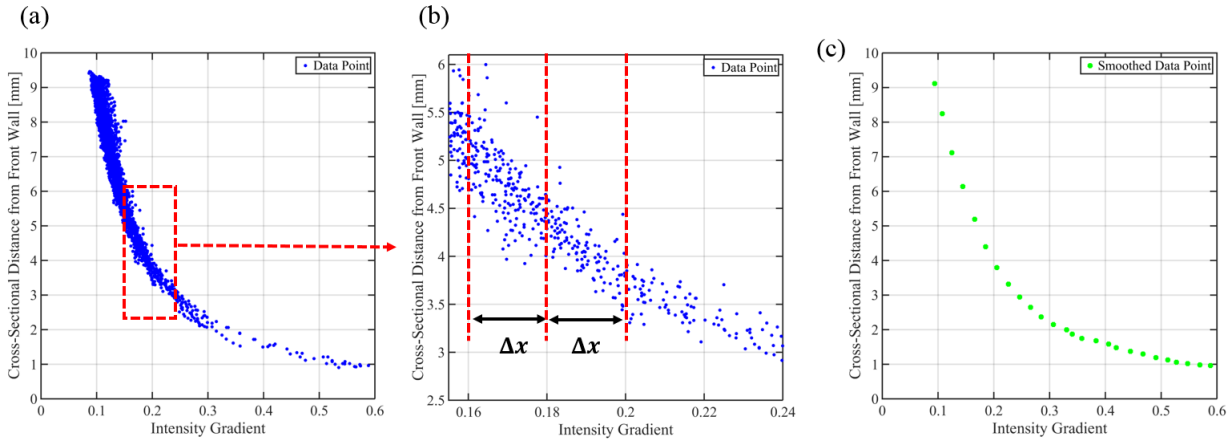

Figure 4.5: (a) Intensity gradient of 3279 bubbles, (b) divided data points with an interval of Δx=0.02, (c) result of averaging the distance and gradient within intervals

As the same manner as the experiment with tube gas injection, the averaged data points are divided into two regions, below or above 4mm. With the averaged data points and Equation (3.3) and (3.4), the coefficients for the two curves are determined and shown in Table 4.2. Figure 4.6 shows the two fitted curves as well as the average data points. Similar to the previous experiment results, the fitted curve above 4 mm agrees with the measured data. As shown in Figure 4.7, the predicted distance has absolute error within ±0.06 mm. In addition, the relative error compared with the averaged measure distances and predicted distances is smaller than 1.0 %. In the case of the predicted curve below 4 mm compared with the averaged measured distances, it has a larger disagreement near the distance of 4.0 mm. Higher absolute and relative errors are shown in Figure 4.7 as the bubble distance approaches the intersection of the two curves.. The highest absolute error is observed around 4.0 mm with about 0.55 mm difference. The relative error at the nearest point to the focal plane and point near the 4 mm are about 11 % and 14.5 %.

Table 4.2: Coefficients for the modeling curves

	C_1	C_2
Curve 1 [0 mm 4 mm]	1.88907	-3.46227
Curve 2 [4 mm 10 mm]	-7.37429	-6.98299

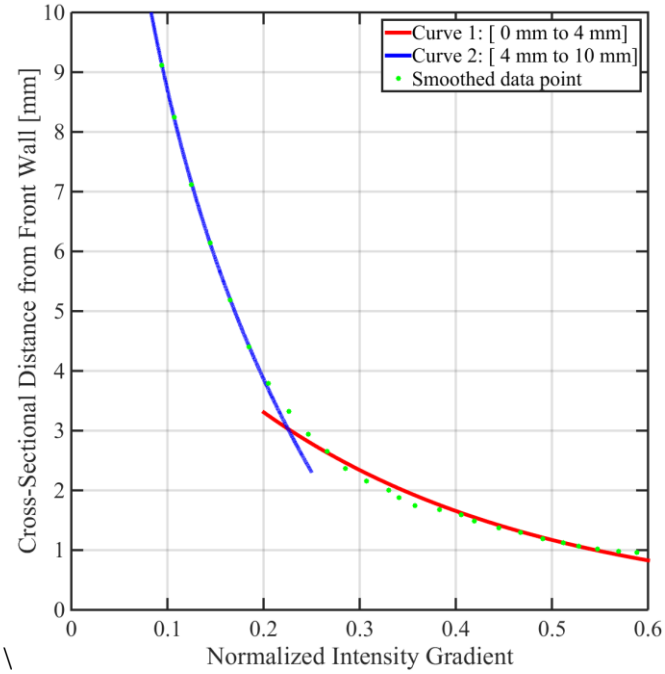

Figure 4.6: Fitted curves for two regions below and above 4 mm with averaged data points

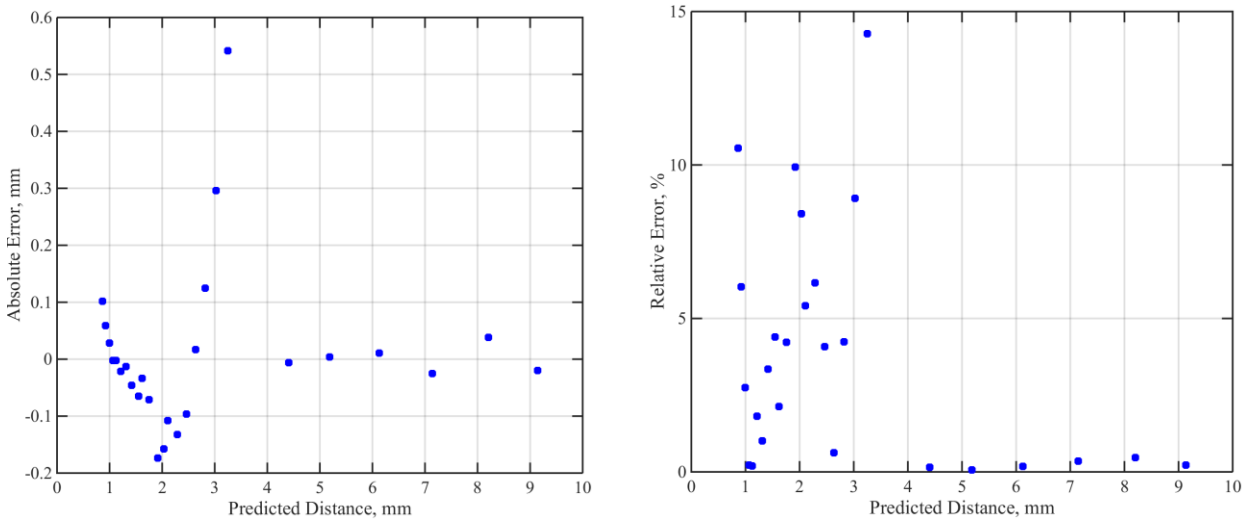

Figure 4.7: (a) Absolute error and (b) relative error

It should be pointed out that when the prediction and individual data points are compared, it shows a reasonable agreement even with the fitted curve less than 3 mm shown in Figure 4.8, but larger differences are observed between 3 mm and 4 mm. Also, it should be noted that larger

uncertainty may exist as the bubble moves farther away from the focal plane. This is evident by the increased scattering of data points near the 10 mm end of the test section. Lastly, other models to predict the bubble distance especially when it moves closer to the focal plane should be considered in order to have a better prediction.

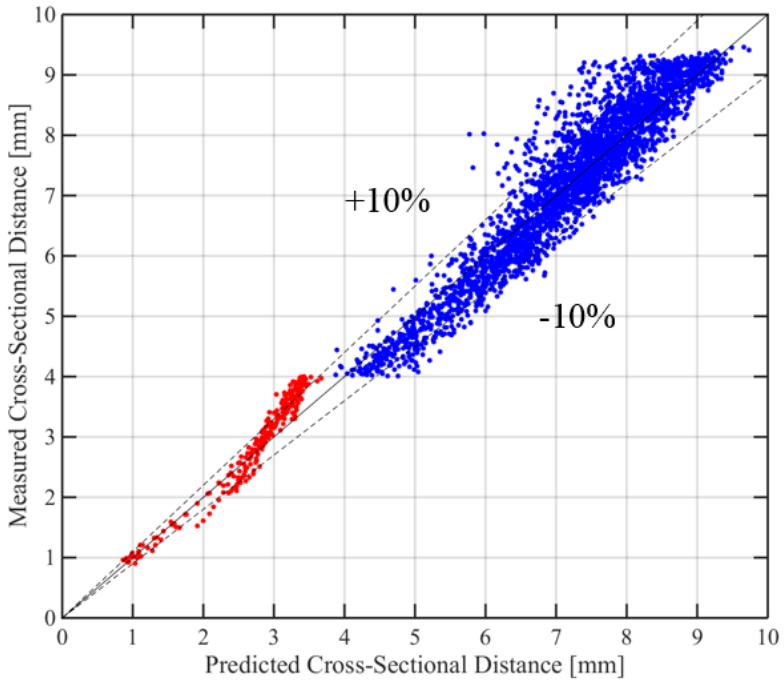

Figure 4.8: Comparison between predicted bubble distances with individual measured values.

Chapter 5

5. Depth of Field Analysis

5.1. Depth of Field

In Chapters 2, 3 and 4, the ball or bubble images are captured and analyzed to predict the distance of the object based on the intensity gradient information using a similar image processing algorithm. However, it should be noted that all three experiment setup and imaging setup are different in some ways. For example, the backlight illumination is different for all cases. The test with acrylic ball images are captured using the high speed camera SA4, which has a resolution of 1024 x 1024 pixels, with 180 mm lens, but the test with a tube gas injection uses the high speed camera SA6 with a resolution of 1920 x 1440 pixels with 180 mm lens. Moreover, the experiment with a single hole gas injection uses SA6 with 105 mm. Then, those three results cannot be simply compared or applied to another test to predict the bubble distance information.

In order to compare results from a different condition, depth of field analysis is introduced here. The depth of field is the range of acceptable sharpness within an object that will appear in focus. So, if an object moves away from the range, the image of the object becomes blurred. In order to derive the depth of field, it is assumed that the thin lens formula can be applied here [31]. Figure 5.1 shows the thin lens model geometry and its model is described as:

$$\frac{1}{d_o}+\frac{1}{s_i}=\frac{1}{f} \tag{5.1}$$

where d_o is the distance from a lens to an object, s_i is the distance from lens to imaging sensor, and f is a focal length of thin lens. Also, the magnification, M is calculated by:

$$M = \frac{h_i}{h_o} = \frac{s_i}{d_o} \tag{5.2}$$

where h_o is an object height and h_i is an object height on imaging sensor. Let the distance between the object and the sensor be L,

$$L = d_o + s_i$$

$$s_i = L - d_o \tag{5.3}$$

Substituting Equation (5.3) into Equation (5.2),

$$M = \frac{s_i}{d_o} = \frac{L - d_o}{d_o}$$

$$Md_o = L - d_o$$

$$d_o = \frac{L}{M+1} \tag{5.4}$$

Then, the distance from lens to imaging sensor is

$$s_i = L - d_o$$

$$s_i = L\left(\frac{M}{M+1}\right) \tag{5.5}$$

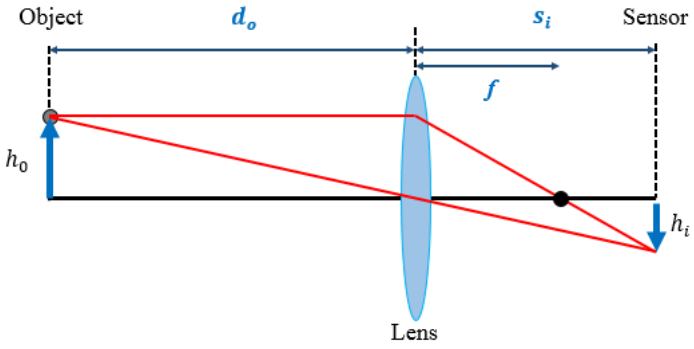

Figure 5.1: Thin lens model geometry

Once the distance from lens to object and the sensor to lens are determined, the depth of field for near side, D_n, and far side, D_f , from the lens position can be obtained using the geometry shown in Figure 5.2:

$$D_n = \frac{Ncd_o(d_o - f)}{f^2 + Nc(d_o - f)} \tag{5.6}$$

$$D_f = \frac{Nd_o c(d_o - f)}{f^2 - Nc(d_o - f)} \tag{5.7}$$

where N is the f-number of lens, c is the circle of confusion which is assumed to be constant as :

$$c = \frac{d_{dia}}{1500}$$

where d_{dia} is the diagonal measure of a camera sensor. The detailed derivation for Equation (5.6) and (5.7) is shown in the Appendix A.

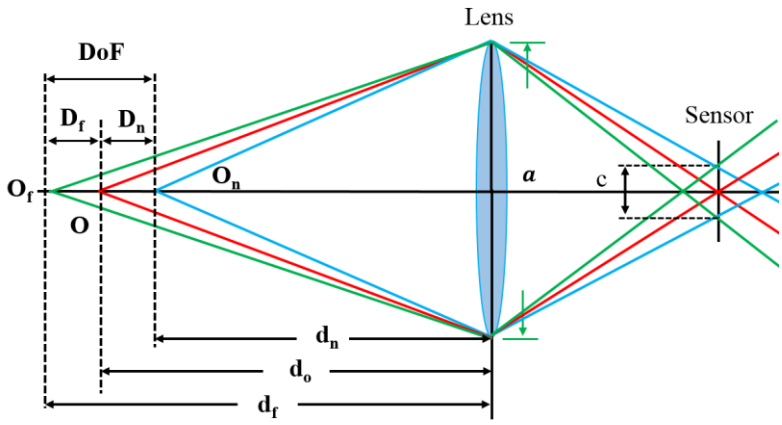

Figure 5.2: Depth of field

5.2. Ray Tracing to modify the DOF

Using the depth of field equation in the previous section and Snell's law, the depth of field can be modified to consider the refraction due to the medium changes through the optical path. Figure 5.3 shows the optical path from the focal plane to the sensor. The red dash line indicates the path of light ray without refraction. The variables shown in Figure 5.3 are as follows:

- d_0 – the distance from the lens to the focal plane
- d'_0 – the distance from the lens to the point if no refraction
- s_i – the distance from the lens to sensor
- a – aperture diameter
- d_a – the acrylic wall thickness, which is 20 mm for this test section
- L – the distance from the sensor to the focal plane

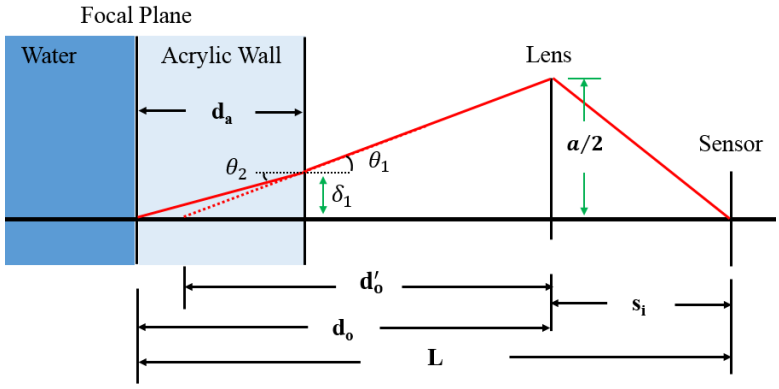

Figure 5.3: Modified DOF at focal plane.

Then,

$$\sin\theta_1 = \frac{\text{Opposite}}{\text{Hypotenuse}}$$

$$\sin\theta_1 = \frac{\left(a/2-\delta_1\right)}{\sqrt{\left(d_o-d_a\right)^2+\left(a/2-\delta_1\right)^2}}$$

Similarly,

$$\sin\theta_2 = \frac{\delta_1}{\sqrt{d_a^2+\delta_1^2}}$$

Using Snell's law,

$$\frac{\left(a/2-\delta_1\right)}{\sqrt{\left(d_o-d_a\right)^2+\left(a/2-\delta_1\right)^2}} = \left(\frac{n_2}{n_1}\right)\frac{\delta_1}{\sqrt{d_a^2+\delta_1^2}} \tag{5.8}$$

where n_1 and n_2 are the refractive indexes of air and the acrylic wall.

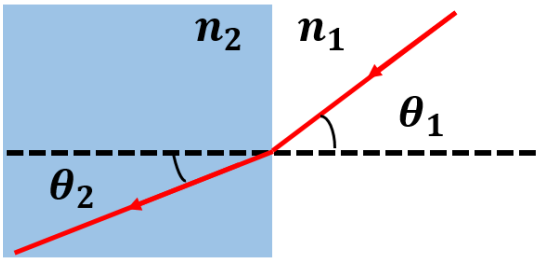

Figure 5.4: Snell's law

Solve the Equation (5.8) for δ_1. Once δ_1 is obtained, the angle of the light ray heading to the acrylic wall is:

$$\theta_1 = \sin^{-1}\left(\frac{a/2-\delta_1}{\sqrt{\left(d_o-d_a\right)^2+\left(a/2-\delta_1\right)^2}}\right) \tag{5.9}$$

Then, d_o' is obtained by

$$d_o^{'} = \frac{a/2}{\tan\theta_1} \tag{5.10}$$

Considering the depth of field for the far side as shown in Figure 5.5, the depth of field for the far side without refraction can be expressed similarly to Equation (5.7),

$$D_f^{'} = \frac{Ncd_o^{'}\left(d_o^{'}-f\right)}{f^2-Nc(d_o^{'}-f)} \tag{5.11}$$

The distance from the lens to the far side of the depth of field without refraction, d_f', and incoming light angle $\theta_{f1}$are calculated as

$$d_f^{'} = d_o^{'} + D_f^{'}$$

$$\tan\theta_{f1} = \frac{a/2}{d_o^{'}+D_f^{'}}$$

$$\theta_{f1} = \tan^{-1}\left(\frac{a/2}{d_o^{'}+D_f^{'}}\right) \tag{5.12}$$

By similar triangle,

$$\delta_{f1} : \frac{a}{2} = \left(d_0^{'}+D_f^{'}\right)-\left(d_0-d_a\right) : \left(d_0^{'}+D_f^{'}\right)$$

$$\delta_{f1}\left(d_0^{'}+D_f^{'}\right) = \frac{a}{2}\left[\left(d_0^{'}+D_f^{'}\right)-\left(d_0-d_a\right)\right]$$

$$\delta_{f1} = \frac{a}{2}\frac{\left(d_0^{'}+D_f^{'}\right)-\left(d_0-d_a\right)}{d_0^{'}+D_f^{'}} \tag{5.13}$$

The angle of the light ray incoming to the acrylic wall and the exiting ray is expressed as:

$$\sin\theta_{f2} = \left(\frac{n_1}{n_2}\right)\sin\theta_{f1} \tag{5.14}$$

$$\theta_{f2} = \sin^{-1}\left(\frac{n_1}{n_2}\sin\theta_{f1}\right) \tag{5.15}$$

Similarly, using Snell's law at the focal plane and letting n_3 be the refractive index of water,

$$\theta_{f3} = \sin^{-1}\left(\frac{n_2}{n_3}\sin\theta_{f2}\right) \tag{5.16}$$

$$\delta_{f2} = \delta_{f1} - d_a \tan\theta_{f2} \tag{5.17}$$

$$\tan\theta_{f3} = \frac{\delta_{f2}}{D_f} \tag{5.18}$$

$$D_f = \frac{\delta_{f2}}{\tan\theta_{f3}} \tag{5.19}$$

Thus, the modified depth of field for the far side is determined by solving the above equations. The DOF for far side is calculated based on each test condition and used to see if the three experimental data sets can be compared in the next section.

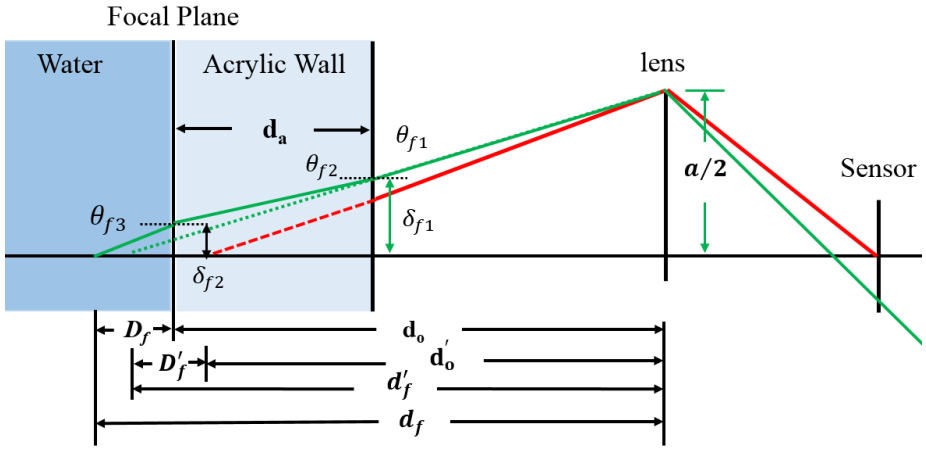

Figure 5.5: Depth of field for far side with refraction

5.3. Results

Table 5.1 shows the comparison of the three different conditions. Also, the modified depth of field for the far side D_f is calculated. Only Test 1 used the SA4 with a resolution of 1024 x 1024 pixels, but the test 1 and 2 used the same lens with a focal length of180 mm. The distance

to the focal plane is different for the three tests as well. Test 3 shows the largest DOF value as compared with the other two values.

Table 5.1: Test condition comparison.

Test #	Test Section	Camera	Distance to focal point [mm]	Lens [mm]	Aperture, N	Conversion [mm/Pixel]	DOF_f [mm]
1	30 x 10 mm	SA4	487	180	3.605	0.0217	0.2023
2	30 x 10 mm	SA6	532	180	4.132	0.0097	0.1629
3	30 x 10 mm	SA6	336	105	9.514	0.0125	0.59692

The measured distances from each test are divided by each DOF value to normalize the distance and to see if the three experimental sets data can be compared. Figure 5.6 shows the normalized distance versus normalized intensity gradient. Test 1 and 2 results seem to merge together as they approach the focal plane. Because of the larger DOF for test 3, the results show smaller normalized distances as compared with the other two experiments. One reason for the difference can be caused by the lens. The focal length is one of the factors to calculate DOF. However, other parameters such as difference in background intensity, conversion ratio, imaging sensor size and etc. or the combination of these can be the reason for the difference. Thus, further detailed experiments and research are necessary to improve the depth of field analysis and compare results with different conditions.

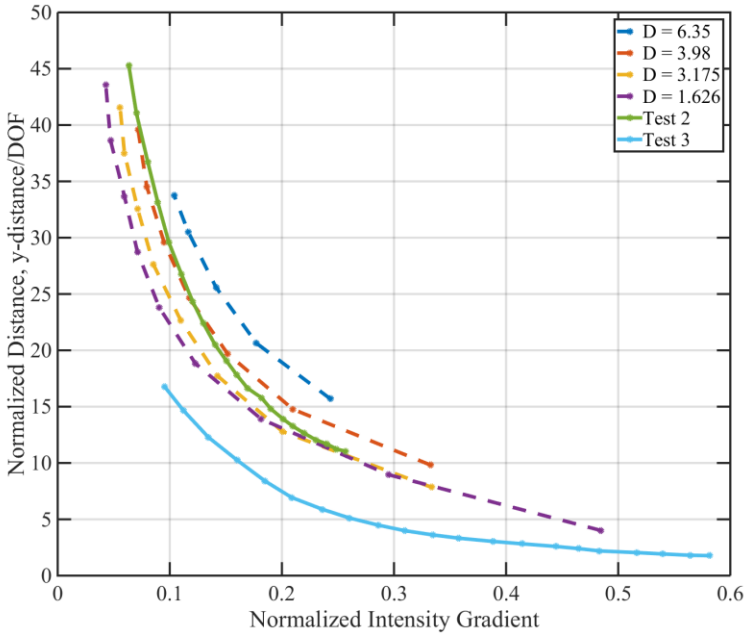

Figure 5.6: Comparison of the test results of the three experiments.

Chapter 6

6. Conclusions and Future Work

6.1. Conclusions

In this thesis, the defocusing technique is applied to two-phase flow measurements in order to extract bubble depth information along the optical path. Also, an image processing algorithm is developed to process images with different flow conditions and extract bubble information such as intensity gradient, outline, area, centroid and depth of the bubble. In the preliminary experiment with solid acrylic balls, it is observed that the distance becomes more sensitive to change in intensity gradient as the ball moves away from the focal plane. Also, the size of the ball affects the intensity gradient value, but it becomes less obvious as the size of bubble decreases. From, the data points, two models are suggested to determine the ball distance to the front wall. The results show acceptable agreement with measured and predicted distances. Then, two additional experiment were conducted one with a tube gas injection and one with a single hole gas injection. In those cases, a log function and an exponential function were used to predict the bubble distance. Also, to capture the tendency found in the first experiment, the collected intensity gradient and bubble distance were averaged. Then, those data points are divided into two regions below and above 4 mm. In both experiments, the fitted curve above 4 mm shows a good agreement with the measured distance having a relative error of 2 % and 1 % for the second and third experiments. On the other hand, the fitted curve below 4 mm shows larger absolute and relative error near the front wall and 4 mm. Based on the two experiments, another model to predict the bubble distance especially when it moves closer to the focal plane should be considered to predict the distance more accurately. The depth of field analysis is introduced to be able to compare three experimental

results. For each experiment, the distance from the imaging senor to the focal plane is divided by the depth of field for the far side calculated with given test conditions. The two experiment using the same lens show similar results but not the experiment data from single hole gas injection.

6.2. Future Work

Currently, the log model used in this experiments shows good agreement with the measured distances when the bubble distance is away from the focal distance. However, as mentioned above the depth estimation mode needs to improve and consider another model to estimate the depth information better. Also, the detailed experiments should be conducted in order to observe how one parameter such as background illumination, the focal length, an aperture size, and camera distance affect one another and the coefficients of the model. Lastly, further investigation is necessary for the depth of field analysis to compare experimental data with different imaging conditions.

References

1. De Lasa, H., S. Lee, and M. Bergougnou, *Bubble measurement in three‐phase fluidized beds using au‐shaped optical fiber.* The Canadian Journal of Chemical Engineering, 1984. **62**(2): p. 165-169.
2. Lim, K. and P.K. Agarwal, *Bubble velocity in fluidized beds: the effect of non-vertical bubble rise on its measurement using submersible probes and its relationship with bubble size.* Powder Technology, 1992. **69**(3): p. 239-248.
3. Kim, S., et al., *Development of the miniaturized four-sensor conductivity probe and the signal processing scheme.* International Journal of Heat and Mass Transfer, 2000. **43**(22): p. 4101-4118.
4. Saito, Y., *Measurement of Interfacial Area Concentration in a Gas-Liquid Two-phase Flow.* JAPANESE JOURNAL OF MULTIPHASE FLOW, 2014. **28**(2): p. 175-182.
5. Da Silva, M.J., et al., *Planar array sensor for high-speed component distribution imaging in fluid flow applications.* Sensors, 2007. **7**(10): p. 2430-2445.
6. Mäkiharju, S.A., et al., *Time-resolved two-dimensional X-ray densitometry of a two-phase flow downstream of a ventilated cavity.* Experiments in Fluids, 2013. **54**(7): p. 1561.
7. Kumar, S.B., D. Moslemian, and M.P. Duduković, *A γ-ray tomographic scanner for imaging voidage distribution in two-phase flow systems.* Flow Measurement and Instrumentation, 1995. **6**(1): p. 61-73.
8. Lindken, R. and W. Merzkirch, *A novel PIV technique for measurements in multiphase flows and its application to two-phase bubbly flows.* Experiments in fluids, 2002. **33**(6): p. 814-825.
9. Bröder, D. and M. Sommerfeld, *An advanced LIF-PLV system for analysing the hydrodynamics in a laboratory bubble column at higher void fractions.* Experiments in Fluids, 2002. **33**(6): p. 826-837.
10. Honkanen, M., et al., *Recognition of highly overlapping ellipse-like bubble images.* Measurement Science and Technology, 2005. **16**(9): p. 1760.
11. Shen, L., et al., *A method for recognizing particles in overlapped particle images.* Pattern Recognition Letters, 2000. **21**(1): p. 21-30.
12. Bröder, D. and M. Sommerfeld, *Planar shadow image velocimetry for the analysis of the hydrodynamics in bubbly flows.* Measurement Science and Technology, 2007. **18**(8): p. 2513.
13. Sommerfeld, M. and D. Broder, *Analysis of hydrodynamics and microstructure in a bubble column by planar shadow image velocimetry.* Industrial & Engineering Chemistry Research, 2009. **48**(1): p. 330-340.
14. Dehaeck, S., et al., *Laser marked shadowgraphy: a novel optical planar technique for the study of microbubbles and droplets.* Experiments in fluids, 2009. **47**(2): p. 333-341.
15. Homayouni, S.S., et al., *Bubble Size Distribution in Oil‐Based Bubble Columns.* Chemical engineering & technology, 2008. **31**(11): p. 1668-1675.

16. Chung, K., M. Simmons, and M. Barigou, *Local gas and liquid phase velocity measurement in a miniature stirred vessel using PIV combined with a new image processing algorithm.* Experimental Thermal and Fluid Science, 2009. **33**(4): p. 743-753.
17. Pentland, A.P., *A New Sense for Depth of Field.* IEEE Transactions on Pattern Analysis and Machine Intelligence, 1987. **PAMI-9**(4): p. 523-531.
18. Hariti, M., Y. Ruichek, and A. Koukam. *A fast stereo matching method for real time vehicle front perception with linear cameras*. in *IEEE IV2003 Intelligent Vehicles Symposium. Proceedings (Cat. No.03TH8683)*. 2003.
19. Scharstein, D. and R. Szeliski, *A Taxonomy and Evaluation of Dense Two-Frame Stereo Correspondence Algorithms.* International Journal of Computer Vision, 2002. **47**(1): p. 7-42.
20. Dhond, U.R. and J.K. Aggarwal, *Structure from stereo-a review.* IEEE transactions on systems, man, and cybernetics, 1989. **19**(6): p. 1489-1510.
21. Chiou, R.-N., et al., *The optimal camera geometry and performance analysis of a trinocular vision system.* IEEE Transactions on Systems, Man, and cybernetics, 1995. **25**(8): p. 1207-1220.
22. Zhigang, Z., et al. *Panoramic virtual stereo vision of cooperative mobile robots for localizing 3D moving objects*. in *Proceedings IEEE Workshop on Omnidirectional Vision (Cat. No.PR00704)*. 2000.
23. Ens, J. and P. Lawrence, *An investigation of methods for determining depth from focus.* IEEE Transactions on pattern analysis and machine intelligence, 1993. **15**(2): p. 97-108.
24. Subbarao, M., T.-S. Choi, and A. Nikzad, *Focusing techniques.* Optical Engineering, 1993. **32**(11): p. 2824-2836.
25. Nayar, S.K., M. Watanabe, and M. Noguchi, *Real-time focus range sensor.* IEEE Transactions on Pattern Analysis and Machine Intelligence, 1996. **18**(12): p. 1186-1198.
26. Xiong, Y. and S.A. Shafer. *Depth from focusing and defocusing*. in *Computer Vision and Pattern Recognition, 1993. Proceedings CVPR'93., 1993 IEEE Computer Society Conference on*. 1993. IEEE.
27. Murata, S. and M. Kawamura, *Particle depth measurement based on depth-from-defocus.* Optics & Laser Technology, 1999. **31**(1): p. 95-102.
28. Stolz, W. and J. Köhler, *In-plane determination of 3D-velocity vectors using particle tracking anemometry (PTA).* Experiments in Fluids, 1994. **17**(1): p. 105-109.
29. MathWorks, I., *MATLAB : the language of technical computing : computation, visualization, programming : installation guide for UNIX version 5*. 1996: Natwick : Math Works Inc., 1996.
30. Otsu, N., *A Threshold Selection Method from Gray-Level Histograms.* IEEE Transactions on Systems, Man, and Cybernetics, 1979. **9**(1): p. 62-66.
31. Hecht, E., *Optics*. 2002: Fourth edition. Reading, Mass. : Addison-Wesley, [2002] ©2002.

Appendix

A. Depth of field calculation

Let the circle of confusion for near DOF be c_n.. Since two triangle $I_nA'B'$ and I_nAB are similar,

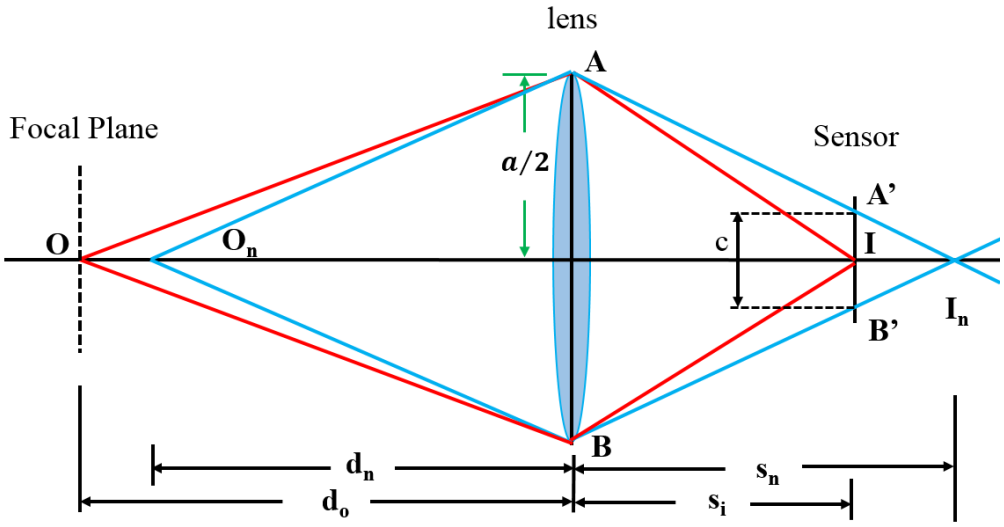

Figure A.1: Near side of the depth of field

$$a : c_n = s_n : (s_n - s_i)$$

$$c_n s_n = a(s_n - s_i)$$

$$c_n = \frac{a(s_n - s_i)}{s_n} \tag{A.1}$$

From the thin lens formula,

$$\frac{1}{f} = \frac{1}{d_n} + \frac{1}{s_n}$$

$$\frac{1}{f} - \frac{1}{d_n} = \frac{1}{s_n}$$

$$s_n = \frac{d_n f}{d_n - f}$$

$$\frac{d_n - f}{d_n f} = \frac{1}{s_n}$$

$$s_n = \frac{d_n f}{d_n - f} \tag{A.2}$$

Similarly, for the distance s_i ,

$$s_i = \frac{d_o f}{d_o - f} \tag{A.3}$$

Substituting Equation(A.2) and (A.3) into Equation (A.1)

$$c_n = \frac{a(s_n - s_i)}{s_n} = \frac{a\left(\frac{d_n f}{d_n - f} - \frac{d_o f}{d_o - f}\right)}{\frac{d_n f}{d_n - f}}$$

$$c_n = \mathrm{a}\,\frac{\left(\frac{d_n f}{d_n - f} - \frac{d_o f}{d_o - f}\right)(d_n - f)(d_o - f)}{\frac{d_n f}{d_n - f}(d_n - f)(d_o - f)}$$

$$= a\,\frac{d_n(d_o - f) - d_o(d_n - f)}{d_n(d_o - f)}$$

$$= a\,\frac{d_o f - d_n f}{d_n(d_o - f)}$$

$$c_n = af\,\frac{d_o - d_n}{d_n(d_o - f)} \tag{A.4}$$

In addition, the aperture diameter, *a*, is expressed as:

$$a = \frac{f}{N} \tag{A.5}$$

where *N is* the f-number of the lens. By substituting Equation(A.5) into Equation(A.4),

$$c_n = \left(\frac{f}{N}\right) f\,\frac{d_o - d_n}{d_n(d_o - f)}$$

$$c_n = \frac{f^2}{N}\,\frac{d_o - d_n}{d_n(d_o - f)} \tag{A.6}$$

Let the circle of confusion for far DOF be c_f. Since two triangles $I_f A'B'$ and $I_f AB$ are similar,

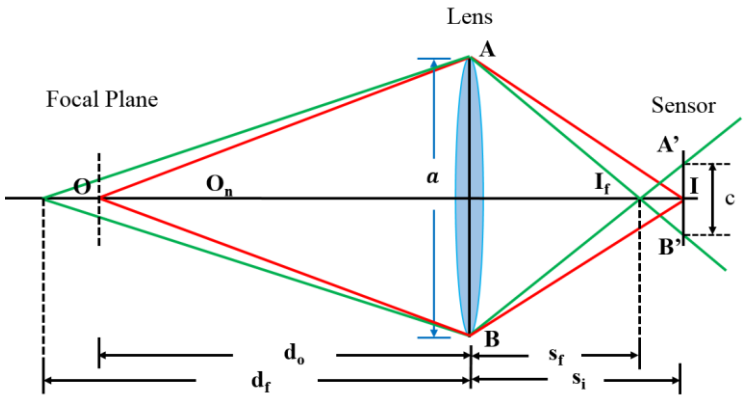

Figure A.2: Far side of the depth of field

$$a : c_f = s_f : \left(s_i - s_f\right)$$

$$c_f s_f = a\left(s_i - s_f\right)$$

$$c_f = \frac{a\left(s_i - s_f\right)}{s_f} \tag{A.7}$$

From the thin lens formula,

$$\frac{1}{f} = \frac{1}{d_f} + \frac{1}{s_f}$$

$$\frac{1}{f} - \frac{1}{d_f} = \frac{1}{s_f}$$

$$\frac{d_f - f}{d_f f} = \frac{1}{s_f}$$

$$s_f = \frac{d_f f}{d_f - f} \tag{A.8}$$

Similarly, for the distance s_i,

$$s_i = \frac{d_o f}{d_o - f} \tag{A.9}$$

Substituting Equation(A.8) and (A.9) into Equation(A.7)

$$c_f = \frac{a(s_i - s_f)}{s_f} = \frac{a\left(\frac{d_o f}{d_o - f} - \frac{d_f f}{d_f - f}\right)}{\frac{d_f f}{d_f - f}}$$

$$= a\frac{\left(\frac{d_o f}{d_o - f} - \frac{d_f f}{d_f - f}\right)(d_f - f)(d_o - f)}{\frac{d_f f}{d_f - f}(d_f - f)(d_o - f)}$$

$$= a\frac{d_o(d_f - f) - d_f(d_o - f)}{d_f(d_o - f)}$$

$$= a\frac{d_f f - d_o f}{d_f(d_o - f)}$$

$$c_f = af\frac{d_f - d_o}{d_f(d_o - f)} \quad \text{(A.10)}$$

Determine the depth of field range toward lens.

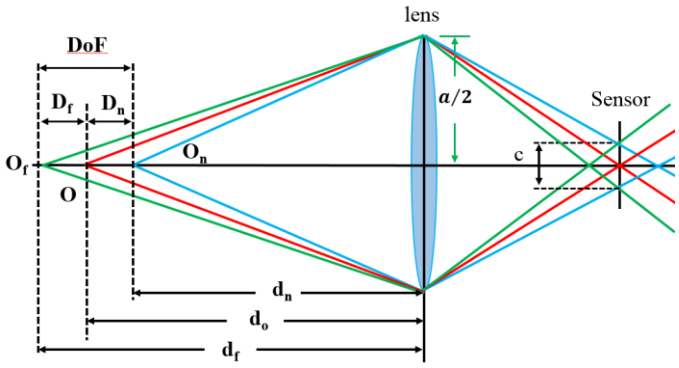

Figure A.3: Depth of field geometry.

It is assumed that the circle of confusion is constant and calculated as:

$$c = \frac{d_{dia}}{1500}$$

where d_{dia} is the diagonal measure of a camera sensor. From Figure A.3, the depth of field for near side, D_n is derived as:

$$D_n = d_o - d_n$$

$$d_n = d_o - D_n$$

$$d_n = d_o - D_n \tag{A.11}$$

Substitute Equation(A.11) into Equation(A.6),

$$c_n = af\,\frac{d_o - d_n}{d_n\left(d_o - f\right)} = af\,\frac{d_o - \left(d_o - D_n\right)}{\left(d_o - D_n\right)\left(d_o - f\right)}$$

$$c_n\left(d_o^2 - d_o f - D_n d_o + D_n f\right) = afD_n$$

$$c_n\left(d_o^2 - d_o f\right) = afD_n + c_n D_n d_o - c_n D_n f$$

$$c_n\left(d_o^2 - d_o f\right) = D_n\left[af + c_n(d_o - f)\right]$$

$$D_n = \frac{c_n\left(d_o^2 - d_o f\right)}{af + c_n(d_o - f)}$$

$$D_n = \frac{c_n d_o\left(d_o - f\right)}{\frac{f^2}{N} + c_n(d_o - f)}$$

$$D_n = \frac{Nc_n d_o\left(d_o - f\right)}{f^2 + Nc_n(d_o - f)} \tag{A.12}$$

From Figure A.3, the depth of field for far side, D_f is derived as:

$$D_f = d_f - d_o$$

$$d_f = D_f + d_o \tag{A.13}$$

Substitute Equation(A.13) into Equation(A.10),

$$c_f = af\,\frac{d_f - d_o}{d_f\left(d_o - f\right)}$$

$$= af\,\frac{\left(D_f + d_o\right) - d_o}{\left(D_f + d_o\right)\left(d_o - f\right)}$$

$$c_f\left(D_f + d_o\right)\left(d_o - f\right) = afD_f$$

$$c_f\left(D_f d_o - D_f f + d_o^2 - d_o f\right) = afD_f$$

$$c_f\left(d_o^2 - d_o f\right) = afD_f + c_f D_f f - c_f D_f d_o$$

$$c_f\left(d_o^2 - d_o f\right) = D_f\left(af - c_f d_o + c_f f\right)$$

$$D_f = \frac{c_f\left(d_o^2 - d_o f\right)}{af - c_f d_o + c_f f}$$

Substituting Equation(A.5) into above equation,

$$D_f = \frac{c\left(d_o^2 - d_o f\right)}{\frac{f^2}{N} - c\left(d_o - f\right)}$$

$$D_f = \frac{N d_o c\left(d_o - f\right)}{f^2 - Nc\left(d_o - f\right)} \tag{A.14}$$